Assessing RADARSAT Constellation Mission sea ice surface topography retrievals using data from ICESat-2

By

Parnian Rezania

B.Sc., Azad University of Esfahan, 2012

M.Sc., Azad University of Esfahan, 2015

A Thesis Proposal Submitted in Partial Fulfilment of the Requirements for the Degree of

MASTER OF SCIENCE in the Department of Geography

in University of Victoria

Supervisory Committee:

Assessing RADARSAT Constellation Mission sea ice surface topography retrievals using data from ICESat-2

By

Parnian Rezania

B.Sc., Azad University of Esfahan, 2012

Dr. Randall K. Scharien, Supervisor

(University of Victoria, Department of Geography)

Dr. Shannon Fargey, Departmental Member

(University of Victoria, Department of Geography)

Dr. Kaan Ersahin, Outside Member

(ASL Environmental Sciences, Inc., Saanichton, B.C.)

Abstract

Recent sea ice dynamics research and ice forecasts focus on the importance of sea ice topography and thickness (e.g., Casey 2018; Dammann et al. 2018; Farrell et al. 2020). Sea ice topography is a critical component in sea ice drag forces, understanding sea ice motion and extent, heat transfer at the ocean-atmosphere interface, and safe ice-related decisions in marine navigation. The overarching objective of this study is to assess the inter-relationships of optical laser altimeter Ice, Cloud, and Land Elevation Satellite-2 (IS-2, 2019-Present) and the C-band frequency RADARSAT Constellation Mission (RCM, 2019-Present) synthetic aperture radar (SAR) to provide near-continual measurements of sea ice topography at the regional scale. For this study, a survey of first-year ice (FYI) and multi-year ice (MYI) in the McClintock Channel portion of the Canadian Arctic Archipelago (CAA) is completed during the winter and spring/summer seasons. RCM ScanSAR mode scenes are regionally co-located with the heights and calculated surface roughness for sea ice from Advanced Topographic Laser Altimeter System (ATLS 07) on IS-2. The IS-2 measured sea ice parameter data provide a vital cross-comparison of RCM measured backscatter variables. An object-based image analysis is used to link the IS-2 measured variables and RCM backscatter quantitatively. For data optimization, 12 bands from RCM are analyzed, including calibrated backscatter channels (HH and HV), their combinations (ratio, addition, subtraction, and multiplication), and a set of grey-level co-occurrence matrix (GLCM) based texture parameters derived from each backscatter channel, following the derivations provided in Scharien and Nasonova (2020). IS-2 ATL07 data are studied to measure sea ice surface elevation and roughness.

Overall, strong positive linear relationships between backscatter and IS-2-derived surface roughness and elevation are found during the late winter (April and May) period, which supports

the use of dual-polarization (HH and HV) RCM scenes and the combination of these channels (HH+HV) as complements to ATL07/IS-2 for understanding winter FYI and MYI ice topography. Generally, RCM derived backscatter is more strongly correlated to IS-2 derived variables than is RCM derived texture. At high incidence angles (>42^{o}) and during late winter conditions, the IS-2 sea ice surface elevation from MYI strongly correlates (r ~ 0.74) with backscatter. However, the correlation between MYI surface height and RCM backscatter during winter is reduced at low and moderate incidence angles (≤42°). The relationship between RCM backscatter and FYI elevation shows a high correlation (r ~0.74 to 0.75) at low and moderate incidence angles. Considering melting conditions, relationships between IS-2 and RCM variables are much weaker compared to winter conditions, though much stronger later in the melting season (July) than earlier (June).

The results of this study suggest that the following techniques should be used to map the elevation of sea ice during the winter using RCM: (1) HH-polarization backscatter (r ~ 0.74) and a low incidence angle (FYI only), and (2) HH+HV polarization (r ~ 0.64) and low incidence angle (MYI only); (3) HH+HV polarization (r ~ 0.74) and high incidence angle (MYI only); and (4) HH-HV polarization (FYI) or HV (MYI) (r ~ 0.75 and 0.72, respectively) and moderate incidence angle. Overall, HH+HV can be the best representative band for FYI topographic investigations using RCM image with low incidence angle during winter.

TABLE OF CONTENTS

List of Tables

List of Figures

Acknowledgements

I gratefully acknowledge the logistical and financial support from my supervisor, Dr. Randall Scharien. I would also like to thank Dr. Shannon Fargey and Dr. Kaan Ersahin for their academic support and encouragement as members of the Master thesis committee. I would also like to thank Dr. Edwin Nissen for fulfilling the role of external examiner for my Master's examination. I am thankful to John Fowler, Diane Braithwaite, and Dr. David Atkinson of the Department of Geography for providing support at the department level. Finally, I am grateful to the administrative staff of the Geography Department and the Faculty of Graduate Studies for logistics.

I would also like to thank Dr. Jessica Fitterer and Dr. Ian O'Connell for their technical expertise and support. Lastly, I am grateful to all members of the ICE lab for their constant support and advice, including Grant John Macdonald, Aikaterini Tavri, Sasha Nasonova, Silvie Cafarella, Vishnu Nandan, and Becky Segal.

Chapter 1: Introduction

1.1. Rationale and Context

Sea ice is a crucial area that occurs by freezing about 10% of the world's ocean's surface water (Leppäranta 2005). The frozen ocean surface of sea ice affects solar energy absorption, atmosphere-ocean heat exchange, and evaporation. Sea ice formation occurs when the atmospheric temperatures drop to below the seawater (salt water) freezing point (-1.86°C) at the onset of winter, usually late September in the Arctic. When thermodynamic congelation ice formation and growth occurs, sea ice eventually consolidates into a coherent ice layer in calm and turbulent conditions. (Weeks and Ackley 1986). The dominant part of the Arctic Ocean is sea ice, specifically during the winter months (see Figure 1.1.). The Arctic sea ice area is located north of latitude 66 degrees.

Over the last several decades, there have been significant declines in the Arctic sea ice cover and its thickness, volume, and age (Perovich. et al. 2019; Hong 2010). The Arctic sea ice extent has decreased by more than 10% per decade since 1979 (see Figure 1.1.), which has consequently increased the sea ice dynamics and drift (Barber et al. 2014). Increasing air temperature in the Arctic has also resulted in increased ice movements and sea ice dynamics in ocean water through enhanced overturning (Lei et al. 2016). The increased dynamics in the Arctic Ocean has lead to the potential for increased sea ice roughness, rubble ice, and sea ice ridges, which are the thickest sea ice features and currently account for about one-half of the total sea ice volume (Leppäranta 2005). Melting sea ice during the summer leads to open water and progressively increases the water temperature, which stores heat and causes further melting of sea ice (Laxon S. et al. 2004). Of note, diminishing the temperature difference between ice and the atmosphere also weakens winds in the jet stream. The weakened jet stream causes more

extreme weather conditions, consequently delaying the ice re-growth during the freezing season, melting, and a slowing rate of re-growth leads to a warmer Arctic, observed to be twice as fast as the global rate (Perovich. et al. 2019). As a result, the topography of the sea ice reflects past thermodynamic and dynamic processes affecting the sea ice cover. Therefore, it is vital to characterize the nature of the surface and define its topographic relief to comprehend changes in the sea ice topography and their influence on other activities at the surface. Surface roughness data can be used to describe the sea ice topography.

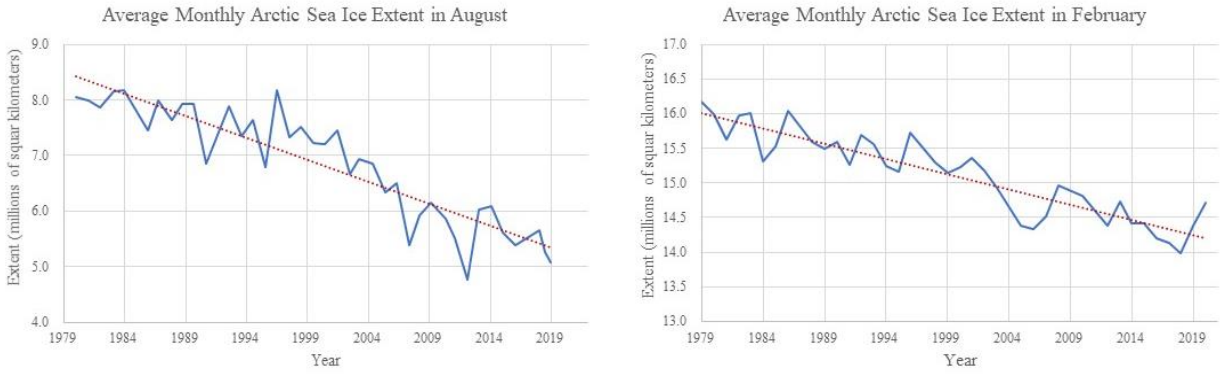

Figure 1.1. The average Arctic sea ice extent for the months of August (left) and February (right) from 1979 to 2019. Data and plots are provided by the National Snow and Ice Data Center (NSIDC). The plots show a trend of approximately 11% decrease per decade (National Snow and Ice Data Center 2019).

In order to support marine activities and conduct long-term climate research, it is necessary to keep track of sea ice conditions, such as ice extent, concentration, topography, and type. Due to the extreme and remote character of the Arctic, remote sensing techniques have emerged as a powerful tool for assessing these features through short revisit times at regional to hemispheric scales. Several studies focus on these features as a source of uncertainty in remote sensing, since they are challenging parameters to retrieve. Twenty countries worldwide have operational ice services that routinely provide sea ice information to fulfill these needs (WMO 2010). These

organizations publish ice and iceberg information products (such as charts, warnings, and forecasts) to facilitate maritime navigation and to record climatic data on sea ice conditions to benefit climate change research (Bertoia et al. 2004). Retrieving sea ice topography, sometimes expressed as surface roughness, is an area of ongoing research. To describe geographical or temporal changes in surface topography from satellite remote sensors, previous techniques have proven too coarse for most applications. Fine-scale observations can be obtained using low-altitude airborne sensors (such as laser altimeters), but the overall geographical and temporal coverage is limited. Therefore, satellite remote sensing techniques are being developed from recently launched sensors that provide fine spatial and temporal resolution.

This primary goal of this research is to develop quantitative relationships between sea ice topography, derived from laser altimeter data, and Synthetic Aperture Radar (SAR) backscatter in both winter and spring/summer months to reflect winter, pre-melt, and advanced melt conditions, respectively. This is achieved by comparing spatially coincident laser altimeter data from the ICESat-2 (IS-2) mission, and SAR data from the RADARSAT Constellation Mission (RCM). The intended benefit of this work is the extension of surface topography mapping, achievable from laser altimeter data but limited to narrow swaths (meter-scale) and infrequent coverage, to RCM and SAR, which provides regular coverage over wide swaths (>350km). Regional surface topography information from SAR are critical to understand sea ice surface characteristics, distinguish between different ice types, determine surface temperatures, estimate surface drag coefficients, and identify marine navigation hazards. This research will support the creation of better monitoring methods for the Arctic sea ice cover, which is experiencing profound change.

1.2. Objectives

The overarching goal of this thesis is to develop SAR technology to map sea ice topography and provide valuable data for sea ice monitoring in support of climate research and, by extension, safe marine operations. In order to conduct the research, IS-2 and RCM data are used to analyze the surface elevation and roughness of the sea ice, as indicators of surface topography, quantitatively. It is crucial to investigate and define the extent to which the level of deformation, represented as surface elevation and surface roughness measurements, affects SAR backscatter. As well, these relationships need to be investigated for various radar system parameters, such as incidence angle, to create SAR satellite-based retrievals models. By using data in different periods of the annual cycle, this study also examines the impact of seasonal changes in surface cover on the relationship between surface topography and observed backscatter. Relationships between backscatter and dry surface cover throughout the winter may not always remain constant during the melt onset and advanced melt seasons, especially when surface melt ponds are present. However, exploring the relationships between winter-derived surface roughness and melt season recorded backscatter is particularly considered to determine what sea ice geophysical information might be recovered under these conditions. This research specifically examines the possibility that data from these sensors may be utilized to:

i. Develop accurate estimates of the topography for both perennial (multi-year) and seasonal (first-year) ice regimes;
ii. Characterize the physical surface roughness of sea ice;
iii. Establish techniques that enable detection of large-scale roughness features that represent a significant risk to marine operations;

1.3. Thesis Structure

This dissertation is comprised of five chapters. The first chapter introduces the research rationale and presents the importance of understanding sea ice characteristics for which better observations could be possible with recent advances in remote sensing technology. The second chapter provides a background on the geophysical characteristics of sea ice, and the relationship between Arctic climate change and sea ice dynamics. Sea ice remote sensing is introduced in Chapter 3, with emphasis on how the geophysical characteristics of sea ice impact measured SAR backscatter, and the application of remote sensing instruments to assess the sea ice topography. Chapter 4 presents the study region, data, analytical strategy, and outcomes, from an evaluation of RCM SAR for sea ice surface topography retrievals using input topography data from ICESat-2. Finally, Chapter 5 summarizes the findings of this thesis, emphasizes their potential relevance, and provides an outlook for future work in SAR remote sensing of Arctic sea ice surface topography.

Chapter 2: Background and literature review

2.1. Sea ice topography and Linear Kinematic Features (LKFs)

Sea ice in the Polar Regions exhibits dynamic processes at large and small scales, with these processes producing ice deformation. The dynamics and deformation processes produce surface characteristics like cracks, and lead to different ice thicknesses. The ice dynamics and deformation effect refer to either ice drag and break, known as *divergence*, or ice-ice interaction, referred to as *convergence* (see Figure 2.1.). When divergence occurs, an ice floe separates along the boundary with another ice floe, which then re-disperses vertically and pulls apart (e.g., Hopkins 1998; Feltham 2008). Significant physical processes include momentum exchange across the air-ice boundary, dynamics forces, heat and salt fluxes, and ice floe size distribution have various feedbacks, each directly or indirectly linked with the deformation and roughness of the sea ice. Traditional definitions of surface roughness include a vertical displacement of the ocean surface from mean sea level, expressed as the standard deviation of relative surface heights within a given area (Beckers et al. 2015). Sea ice motion determines the roughness; when dynamical forces, particularly wind and ocean current, increase, the roughness increases. In other words, ice surface characteristics that suggest increased roughness and agitated region have been warped by ice motion forces.

Sea ice typically consists of areas of level ice and deformed ice including ridges, separated by cracks called fractures and/or leads, all with different spatial scales (Petty et al. 2016). Quasi-linear areas of open water between divergent ice floes are referred to as leads (Haas 2010). Leads can be created in pack ice at any time of year; however, leads refreeze rapidly in winter. When convergence occurs, ice floes are forced together by means of pressure driving forces, resulting in vertical displacement and quasi-linear structures called pressure ridges or, simply,

ridges. Ridges consist of a top side from ice level to the peak, known as a *ridge sail*, and a bottom part below the water level, termed an ice *keel* [Figure 2.1.] (Haas 2010). The keel draft to sail height ratio is approximately 4.5:1. Pressure ridges are easily distinguishable from smooth first-year ice (FYI), however, the surface of the deformed MYI can be made of sails and rubble fields, masking the appearance of new or recently formed ridges (Petty et al. 2016). Note that the size, form, and location of described structures significantly depend on the forces exerted on the ice floes during, and after, the formation process. For instance, divergence can typically open a crack, while convergence closes the crack. First-year ridges are defined as those which have not survived one summer's melt. First-year ridges may present very sharp sails with visible blocks, and their degree of consolidation is almost always much less advanced than the older multi-year ridges (Strub-Klein and Sudom 2012).

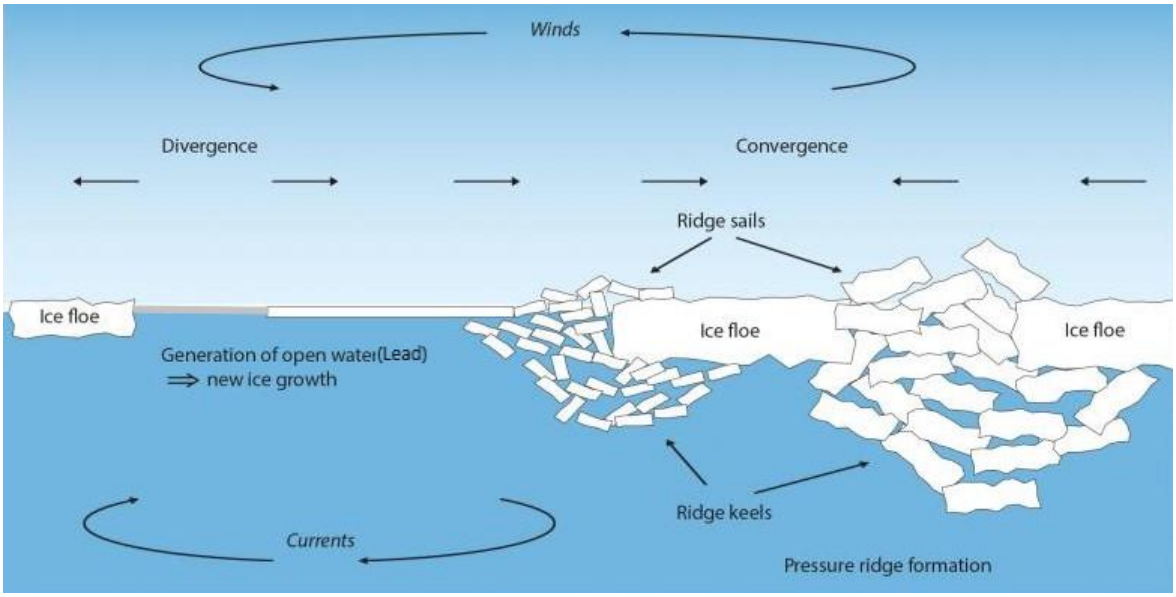

Figure 2.1. Illustration demonstrating the dynamics forcing processes that diverge or converge sea ice floes and alter ice thickness (Haas 2010).

Focusing on sea ice features resulting from ice dynamics, both pressure ridges and leads are called Linear Kinematic Features (LKFs), particularly due to their quasi-linear, elongated shape (Hutter, Zampieri, and Losch 2019), as well as the kinematic processes (opening, closing, shear,

or a combination of thereof) associated with their formation (Kwok 2001). LKFs are long and narrow features, consisting of open water (e.g., leads), nilas, new ice, young-ice, FYI, ridge ice, or rafted ice. LKFs have been observed at various scales, ranging from a few meters in aerial photographs to basin-wide scales in satellite imagery. Different directions of the kinematic formation processes change the resulting shapes of LKFs, whereas the different directions of ice floe motions dictates the LKFs characteristic shape in a short time after the creation procedure (Schulson and Duval 2009). Ice floe edges and open water between ice floes in some cases may make LKF patterns that are hardly distinguishable.

The study of sea ice roughness and thickness, both indicators of topography, are important because topography:

i. Affects the form of drag on the upper and lower surfaces of the ice, attributed to the variation of ice surface roughness *via* its impacts on the momentum balance and divergence/convergence of sea ice (Tsamados et al. 2014).
ii. Affects sea ice melt patterns by determining the location and extent of surface melt ponds during summer (Perovich and Polashenski 2012). Fewer melt ponds have been seen on rough ice where the ice-albedo is higher than on smooth ice where shallow melt ponds broadly expand over the ice surface;
iii. Affects gas exchanges between the atmosphere and the ocean and the flux of heat (Wadhams and Comiso 1992);
iv. Controls the mass flux of sea ice out of the Arctic region, as defined by a combination of ice thickness and ice velocity. This is a critical factor for quantifying the redistribution of freshwater between the polar and sub-polar seas (Kwok 2010); and

v. Impacts marine transportation and navigation, important offshore structures, and economic development (Sudom et al., 2011; Timco and Weeks, 2010). Local to regional scales measurement of ice thickness is vital in order to monitor and report sea ice conditions in near-real time marine navigation and transportation (Geldsetzer et al. 2015).

2.2. Arctic climate change and sea ice dynamics

Sea ice is known as a climate indicator (Haas et al. 2009) because of the importance of its dynamics and development in observing global climate change. Sea ice and ocean surface roughness variations have become crucial variables in climate study and monitoring due to the dramatic sea ice loss in recent years. In addition, the dipole spatial structure of recent sea ice fluctuations might be affected by dynamical variables that could affect temperature and precipitation over land patterns (Fissel, Marko, and Melling 2015). The distributions of sea ice features control the global energy balance (Curry, Schramm, and Ebert 1995), local winds, ocean currents, Coriolis and internal forces, and sea surface tilt. Similarly, wind forcing, ice-water drag, and Coriolis affect ice motion and dynamics (Lei et al. 2016). In addition, ocean currents have been gradually separated and altered due to gravity, making sea surface tilt another major ice-movement driving force.

Arctic climate change causes shorelines to experience fall storms when coastal ice does not form at the anticipated period, which leads to erosive behaviours. It also enhances thermal subsidence of coastal permafrost, therefore greatly accelerating the rate of coastal retreat over time (Eicken and Mahoney 2015). The outcome of sea ice extent and dynamics changes are the same as enhanced coastal erosion and broad threats to coastal infrastructure. Their scales fall between regional to hemispheric scale, and at the local scale with regional to global repercussions.

Sea ice divergence creates more open water area, decreasing surface albedo and increasing the surface air temperature by exposing open ocean. When sea ice converges, ice floes collide or break, resulting in the creation of thicker ice features and/or more ice floes and higher albedo. Reduction of the albedo and increasing air temperature decrease the sea ice extent, where older ice melts in summer, and newly formed ice appears during the onset of freezing. Younger ice (i.e., FYI) can then exceed old ice (i.e., MYI) coverage across the Arctic. Less ice extent and more drift ice have also enhanced the elevation of marine traffic and hazards (Pizzolato et al., 2014). During the fall storms, an increase in wave heights and deeper propagation of swell into the spring ice pack can result in thinner and more dynamic ice (O. P. Francis and Atkinson 2012). Thus, wave action and warming of surface waters promote the thermal sub-erosion of both terrestrial and marine permafrost along the coast. These changes have some consequences, such as the acceleration of coastal retreat rates with possible adverse effects on coastal communities and infrastructure, as well as an increase in erosive action and thermal sub-erosion of coastal permafrost.

With declining sea ice extent, ecosystem impacts, and increasing economic interests in the Arctic, the need for monitoring and predicting sea ice characteristics has increased. Determining LKFs and understanding their spatial and temporal evolution is vital in order to generate sea ice and ocean models and to evaluate sea ice deformation with high spatial resolutions (Mohammadi-Aragh et al., 2018). Recent sea ice forecasts mainly focus on pan-Arctic quantities such as sea ice extent and thickness. Leads are critical for determining the sea ice freeboard and thickness (Farrell et al. 2020), understanding sea ice melt, as well as for marine navigation. Leads are open water or have thinner ice after winter, making them easy to traverse. Ridged ice is stronger than level ice or refrozen leads (AMSD 2018), making pressure ridges a critical

hazard in marine usage. Pressure ridges indicate high pressure and a highly dynamic region, which consequently leads to high albedo. Therefore, detecting LKFs during the winter can promote sea ice predictions.

Sea ice can be a significant hazard through direct interactions of properties and infrastructure, the indirect impacts of variability, and rapid changes in its distribution in Arctic regions. Due to the significant impacts of climate change on the marine cryosphere, accurate monitoring of the Arctic sea ice topography is of fundamental importance (Geldsetzer and Yackel 2009). Sea ice topography is a broad term that encompasses surface roughness, which may include LKFs such as ridges, and is generally related to thickness. Knowledge of sea ice topography is essential, along with the location of ice floes, ice edge (the boundary between the ice and open water), and the presence of LKFs in the context of critical strategic and technical information for marine users. Studying the sea ice surface roughness provides a signal of the mechanical deformation history of the ice, which the knowledge of it is required to understand the exchange of turbulent energy between the ice and atmosphere and drag-induced ice dynamics (Zwally et al. 2002). The location of these parameters also enables recognizing the safe (i.e., ice-free area) and/or hazardous pathways for marine activity (Ramsay et al. 1993; Scheuchl et al. 2004; MSC 2005). The significant variation in the Arctic sea ice conditions and increased marine activity will most likely lead to an increase in demand for ice information products promoting marine stewardship and enhancing safety in the coming decades (Pizzolato et al., 2014). These products are applicable for operational ice services, including the Canadian Ice Service (CIS). Ice services are typically interested in promoting the accuracy, information content, and production efficiency of their ice information products. In particular, ice services are able to enhance ice analysis charts, including information on sea ice extent, stage of development (i.e., ice type), and predominant

form (i.e., pressure ridges size, leads size, and ice floe size) in a near-real-time basis and different scales.

CHAPTER 3: Remote Sensing of Sea Ice Topography

3.1. Overview of Current Remote Sensing Instruments and Techniques

Remote sensing of sea ice parameters include ice type, concentration, extent, thickness, deformation state, and melt onset and freeze up. The majority of satellite Earth observation systems include visible/infrared (VIR) sensors, passive microwave radiometers, and radar/SAR (Eppler et al. 1992; Meier 2005; Heinrichs, Cavalieri, and Markus 2006), all of which acquire complementary information on various scales. Optical sensors enable discrimination between sea ice and open water, based on their contrast in albedo. Although these spectroradiometers can give outstanding multi-spectral details and fine surface spatial resolution, they are constrained by clouds and rely on sunlight. Specific applications for sea ice monitoring in Polar Regions are thematically related to optical imagery with several visible and infrared channels (Shokr and Sinha 2015). The cloud and darkness limitations are eliminated by moving to the microwave portion of the spectrum. Microwaves can penetrate clouds and enable unrestricted monitoring from the Earth's surface, enabling detection at any time of day or night (McCandless Jr. W. Samuel and Jackson, 2004). Passive microwave and thermal infrared sensors utilize the difference between ice and water microwave emissivity and the difference in the physical temperature. Long wavelength (low frequency) microwaves have a low energy content, hence the energy that is accessible is relatively low and needs a wide field of view to be detected. The majority of passive sensors are frequently constrained by this to have relatively poor spatial resolutions. However, the poor spatial resolution frequently allows for a broader areal coverage, which has been essential for mapping the densities of sea ice over the whole. Active remote sensing systems, on the other hand, are self-sufficient in terms of their energy source for lighting and are not reliant on the electromagnetic (EM) radiation from the Sun or the Earth's temperature

characteristics. The technology uses an antenna for both transmission and reception. Radiation is directed towards a target by the transmitter, and the receiver picks up radiation that the target has backscattered. Active sensors have the benefit of being able to detect surfaces at any time, regardless of the day or the time of year. They also have the advantage of being able to study wavelengths that the sun does not properly offer and of being able to better regulate how bright a target is illuminated (Richards 2009). Additionally, active sensors can attain a far better spatial resolution (described further in the next section).

Active microwave, also known as radar, an acronym for Radio Detection and Ranging (Ager 2013), provides its own energy source to produce an image (Inggs and Lord 2005). Although it is similar to emission, the backscatter of microwave energy emitted from sensors is strongly influenced by the phase state and salinity, with sea ice typically scattering more energy than the ocean, unless there is significant wind-wave action (Tedesco 2015).

By observations from different study methods, many algorithms for sea ice parameter retrieval have been created based on the difference between the physical and radiometric features of sea ice and open water (Shokr and Sinha 2015). SAR sensors capable of acquiring data at more than one polarization are currently the most state-of-the-art in radar imagery acquisition technology from satellites (e.g., RADARSAT-2 and RADARSAT Constellation Mission). Although SAR sensors detect a wide range of measured backscatter values under some circumstances, for example, variable wind-wave conditions on water surfaces, this technology is capable of distinguishing sea ice and open water when multiple polarizations are used (Geldsetzer and Yackel 2009). The potential use of SAR for sea ice topography and LKF detection is covered in the next section.

Numerous methods have been developed to retrieve sea ice topography and individual LKFs. However, the most detailed datasets of sea ice topography and LKFs are from airborne platforms, with data from surface profilers and laser scanners normally used to enhance the understanding of their spatial and temporal nature (Strub-Klein and Sudom, 2012; Castellani et al., 2014). Profiling laser data, typically from sensors mounted on aircraft, have historically enabled the identification of level ice and ridges, ridge widths (along the profile line) and sail heights (e.g., Hibler 1972; Dierking 1995). Analyzing laser profiler data was improved with a multi-step filtering process and elimination of aircraft altitude variations from laser range measurements (Hibler 1972). The advent of inertial navigation systems (INS) improved the derivation of surface data and the removal of aircraft motion. The outcome is an outline of ice surface height defined relative to the minimum local height, normally the local height of level ice, along the laser profile. At this point, ridges are determined from the local maxima using the Rayleigh criterion, and leads as local minima.

Ice surface roughness and LKFs can also be derived from Airborne Laser Scanner (ALS) data and airborne Very High spatial Resolution (VHR) optical imagery. Point cloud or gridded elevation data can be derived from ALS data, which results in the ability to discriminate ridged ice and quantify surface topography, e.g. by calculating ridge density or surface roughness (Casey 2018). Point cloud data also can be derived from VHR by using Structure from motion (SfM) technique, resulting in three/four-dimensional sea ice topography and LKF information (Micheletti, Chandler, and Lane 2015; Chudley et al. 2019). SfM photogrammetry reveal visible points at known three-dimensional positions by defining internal camera geometry and camera position and orientation (Westoby et al. 2012). However, ALS data and VHR airborne imagery can not cover annual development, and they are mostly limited to small swaths below the flight

line of the aircraft (Petty et al., 2016). The use of Autonomous Underwater Vehicle (AUV) sonar along with airborne laser profiling to analyze sea ice morphology is another tool for studying sea ice topography (Doble et al., 2011; Williams et al., 2015). However, though AUV and laser scanner data provide high-resolution and three-dimensional observations of ice conditions in near-real time, data are limited and costly, and the estimated parameters like ice thickness are not well suited for regional-scale climate studies or marine operations. Moored upward looking sonar sensors, also known as ice-profiling sonars (IPS), provide time series sea ice draft data at a fixed point, for monitoring local ice draft distributions related to sea ice dynamics and seasonal growth and melt conditions (Fukamachi et al., 2017).

In terms of satellite data, space-based altimeters with polar orbital inclinations are equipped to monitor Earth's polar regions, including Ice, Cloud, and Land Elevation Satellite (ICESat, 2003–2009), CryoSat-2 (CS-2, 2010–present), SARAL/Altika (2013-present) and IS-2 (2019-present). Together they have provided near-continual wintertime measurements of sea ice topography at the basin scale (e.g., Laxon et al. 2013; Petty et al. 2020). Note that, ICESat was a green and infrared laser altimeter, IS-2 carries a green laser altimeter, while CS-2 and SARAL/Altika carry Ka-band and Ku-band frequency radar altimeters, respectively (Kwok et al. 2009; Laxon et al. 2013; Kwok et al. 2019). From these altimeters, ice thickness algorithms have been developed based on their different sensitivities to inputs of snow depth (Zygmuntowska et al. 2014) and different sensor technologies. The ice thickness algorithms are based on the measurement of sea ice freeboard, the height of the snow surface (in the case of IS-2) or the ice surface (in the case of **S**atellite with ARgos and ALtiKa (SARAL/Altika) and CS-2) relative to the height of the local ocean surface. In comparison to earlier/existing altimeters, SARAL's technical features make it a better choice, especially for ice surface research (Remy, Legresy,

and Vincent 1999). For example, the SARAL/AltiKa altimeter indicates a proper correlation with detecting leads and monitoring their spatio-temporal dynamics during winter (Zakharova et al. 2015). The recovery of sea ice thickness is one of the specific research goals of CS-2 spaceborne altimeter system (Drinkwater et al. 2004). The mission objective for the CS-2 sea ice thickness retrieval is to determine the rate of ice thickness changes of the whole Arctic sea ice pack (Francis 2007).

3.2. Sea ice remote sensing using SAR

Three types of radar instruments, including scatterometer, radar altimetry, and imaging radar i.e. SAR, are applicable in sea ice studies. Image data can also be created from the scatterometer observations. Scatterometer systems primarily measure wind speed and direction over the ocean, but are also applicable in monitoring sea ice in the Polar Regions (Remund and Long 1999; Casey et al. 2016). Radar altimeters are nadir-looking instruments used for topographic mapping of glaciers and ice shelves. They have been used to estimate sea ice thickness and surface topography in Polar Regions (e.g. Chelton and Wentz 1986; Rémy and Parouty 2009). Data from imaging radar systems are frequently applied to monitor sea ice (Shokr and Sinha, 2015). An antenna emits microwave energy pulses and uses the reflections to create images (Ager 2013).

Imaging radar systems, also known as SARs, have a resolution that does not degrade with distance (Ager 2013) and create high-resolution (meter-scale) images of the Earth's surface with remarkable characteristics (Inggs and Lord 2005). SAR helps all the measurements of orbital motion, range, amplitude, and phase be done with the highest precision, regardless of clouds and distance (Ager 2013).

The SAR sensitivity to surface roughness on the centimeter to decimeter scale suggests that it may be possible to estimate the surface height statistics of both deformed and level ice if a

suitable model is established (Carlström and Ulander 1995). Using radar remote sensing to identify and understand sea ice roughness and deformation on micro and macro scales is cost-effective. In particular, SAR is the primary data source for ice charting and provides a high temporal and precise record of sea ice changes, trends, and variability (Comiso and Hall 2014).

Previous studies showed that SAR data, under certain conditions, provide many practical sea ice observations, including the contrast between different ice types, ice/open water (hence open leads), ridging, ice drift tracking, and frost flower formation areas (Dierking and Busche 2006; Arkett et al. 2008; Dierking 2010b; Casey 2018). SAR data have been used for different tasks for tactical scale monitoring at finer spatial resolution and ship navigation. Examples of SAR tasks include ice type classification (Nghiem and Bertoia 2001), determination of the ice drift pattern from consecutive images (Sun 1996), observations of marginal ice zones (MIZ) (Livingstone and Drinkwater 1991) and polynyas (Drucker 2003), information gathering about lead characteristics (Van Dyne, Tsatsoulis, and Fetterer 1998), monitoring of melt onset and freeze-up (Winebrenner, Holt, and Nelson 1996), retrieval of parameters characterizing the ice surface topography (Similä et al. 1992), improvement of thin ice type discrimination (Kwok et al. 1995), and estimation of ice thickness (Haverkamp, Kiat Soh, and Tsatsoulis 1995).

SAR backscatter is affected by the radar system parameters and the surface (e.g., sea ice or open water) geophysical and EM properties (Onstott 1992). The former includes radar frequency, polarization, incidence angle, and noise-equivalent sigma-zero (Onstott 1992). The latter is especially affected by warming conditions, liquid water within the snowpack, and/or melt ponds and lead formation. Melt can undesirably hide the backscatter signature of underlying sea ice, especially during melt onset, when the surface is covered with wet snow, and the backscatter signatures of FYI and MYI undergo extreme variations (Arkett et al. 2008). Overall,

the difficulty of estimating the surface backscatter of the Arctic sea ice during melt has generated a wide range of published studies (Laine et al., 2011).

According to previous studies, decreasing the SAR frequency leads to a lower sensitivity of backscatter to snow and ice variations, and a higher backscatter sensitivity to large-scale sea ice surface roughness (e.g., ridged ice) (Dierking and Busche 2006; Dierking 2013). In addition, the incidence angle and ice surface roughness directly correlate with backscatter. Smoother ice surface results in significantly decreased backscatter as a function of increasing incidence angle, whereas deformed ice generates diffuse surface scattering and multiple-bounce surface scattering, which results in strong backscatter at all incidence angles. Thicker ice (i.e., MYI and ridged ice) can have volume scattering, which also contributes to strong backscatter at all incidence angles. Usage of multi-polarization SAR data has further enhanced sea ice backscatter characterization and feature identification (e.g., Scheuchl, Cumming, and Hajnsek 2005; Eriksson et al. 2010; Kim, Kim, and Hwang 2012; Gill and Yackel 2012; Fors et al. 2016; Johansson et al. 2017). In addition, a wide swath of single- and dual-polarized SAR data has been employed to assess sea ice extent, concentration, and ice type. Co-polarized data, HH and VV, enhanced differentiating the targets due to their sensitivity to multiple-surface roughness scattering (Oh, Sarabandi, and Ulaby 1992). HV and VH backscatter from sea ice are affected by surface roughness, volume scattering, and multibounce scattering. At steeper incidence angles, the ice-ocean contrast of HV or VH can be expected to be greater than that for either of the co-polarization channels (Nghiem and Bertoia 2001).

There have been limited studies regarding sea ice topography and LKF detection from SAR, with most of the focus on detection during cold, winter-like conditions (Casey2018). Roughness is a relative notion in SAR remote sensing that depends on the wavelength and incidence angle.

A surface is considered "rough" from the standpoint of scattering physics if its structural characteristics have dimensions similar to the incident wavelength. The Rayleigh criteria state that a surface is smooth if

$$h < \frac{\lambda}{8 * \cos\theta}$$

And is rough if:

$$h > \frac{\lambda}{8 * \cos\theta}$$

Where h refers to the mean height of surface variations, λ refers to the radar wavelength, and θ denotes the radar incidence angle.

The threshold at which a surface becomes rough enough to backscatter is described by the Rayleigh criteria. In the case of pure surface scattering, the amount of backscatter rises as the surface grows rougher. In the sections that follow, it will be discussed how well-suited a SAR sensor is for a specific task of monitoring depending on frequency, incidence angle, and polarization.

3.2.1. Frequency (Wavelength)

Radar imaging depends on the frequency and its penetration depth, with lower frequency having greater penetration. Consequently, the volume contribution to the backscattered signal is often amplified in the low frequency case. Radar frequency bands are designated in frequencies ranging from 0.3 GHz (UHF) to 300 GHz (mm), with SAR imaging systems refraining from wavelengths less than 1.11 cm (K-Band) because energy is reflected by water vapour and other atmospheric particles. To find rain and storms, Doppler radar weather equipment employs

high-frequency microwave bands (greater than 27 GHz) because of this property. Therefore, SAR imaging systems for Earth observing often employ the imaging bands X-, C-, L-, and P-band (Ager 2013; Moreira et al. 2013). Table 3.1 lists the SAR bands' corresponding wavelengths and frequency ranges.

Table 3.1. The Frequency bands for SAR systems and the corresponding frequency and wavelength ranges (adopted from Moreira et al., 2013).

SAR Radar Band	Frequency Range [GHz]	Corresponding Wavelength Range [cm]
Ka	40–25	0.75–1.2
Ku	17.6–12	1.7–2.5
X	12–7.5	2.5–4
C	7.5–3.75	4-8
S	3.75-2	8-15
L	2-1	15-30
P	0.5–0.25	60-120

According to experimental and model results of sea ice over all seasons, backscatter is caused mainly by the roughness of the snow-ice interface at C- and X-band. On the other hand, backscatter returns from the sea ice interior can come from the L- and P-band frequencies because of their greater penetration depth. Therefore, C-band SAR imaging capability is a reasonable compromise between the use of shorter wavelengths (X- and Ku-band) and longer wavelengths (L- and P-band) (Dierking and Busche 2006). In addition, only C-band waves interact with the ice's surface and subsurface elements such as ridge blocks, ice fragments, and small-scale surface roughness. Other frequencies have not been used as frequently for sea ice imaging as C-band, and there is much expertise in their usage (Dierking 2010a).

Most sea ice-related studies have focused on the characterization of C-band backscatter related to various parameters. Deformed, level and new ice areas were separated using C-band SAR data (Nghiem and Bertoia 2001). C-band SAR imagery is used operationally to differentiate between FYI and MYI types and to distinguish between areas of open water and sea ice (Arkett et al., 2008; Casey, 2018). C-band SAR was also demonstrated to make detecting sea ice pressure ridges easier compared to higher frequencies (Onstott 1992; Dierking and Busche 2006). Therefore, the C-band SAR shows more reliable results in sea ice roughness and topography, ridge detection (e.g., Cafarella et al., 2019), and lead detection (e.g., Gupta et al., 2019; Murashkin et al., 2018).

3.2.2. Incidence angle

The energy from a SAR is transmitted and received at different angles relative to the sea ice surface. Smaller angles are closer to perpendicular to the terrain, and more extensive angles are closer to parallel, and these incidence angles are measured relative to an imaginary line perpendicular to the sea ice surface [Figure 3.1.] (Jensen 2000). Every SAR instrument includes a variety of beam modes that enable it to image the Earth at varying incidence angles and swath widths (usually ranging from 15 to 65 degrees)(Facility et al., 1996; Mladenova et al., 2013). It becomes more challenging to interpret SAR imagery because of the incidence angle effect on the backscatter properties of sea ice. (Lang et al., 2016). Though the strength of backscatter from the surface depends on the surface roughness and the dielectric constant, the backscatter also declines as the incidence angle increases.

Understanding the EM characteristics of each component of sea ice is crucial to interpret backscatter. Surface roughness estimation using SAR remote sensing techniques is still in

development. The volume of rough ice or the surface itself may affect signatures at considerably smaller temporal and geographical scales than those represented by the incoming EM waves from the satellite. Understanding the EM wave scattering mechanisms from sea ice is crucial to studying the roughness of the sea ice surface. The measurement of the EM absorption, reflection, and scattering of sea ice is the dielectric constant (Morey, Kovacs, and Cox 1984). Surface scattering occurs at boundaries between materials with contrasting dielectric constants (e.g. air and water), when the surface roughness also becomes a factor. When examining volume scattering, individual scattering may occur at different dielectric discontinuities within the volume (Richards 2009). When the active microwaves interact with a target, there can be volume scattering within the target before the return EM wave is released. This sub-surface scattering can occur when some of the incident waves penetrate the surface slightly, and scattering occurs within the volume of a roughness feature at the surface like ridges and ice blocks at the surface of the sail.

The backscatter from a rough surface is in general expected to decrease with increasing incidence angle, and rougher surfaces make the backscatter more random (M. Mäkynen and Hallikainen 2002). The rougher surface shows the brighter backscatter on the image. The slope of decreasing backscatter is dependent on sea ice type (Onstott 1992). For example, in the study of pressure ridges expected to have brighter returns at higher incidence angles (H. Melling 1998). Surface scattering predominates at incidence angles less than 45^{o}, whereas volume scattering from FYI at C-band is only discernible at shallow incidence angles (Carlström and Ulander, 1995; Dierking, 1999). On the other hand, the increase of incidence angle ($>45^{o}$) can cause undulations of the uneven observed waveforms. These are caused by fading effects and/or by inhomogeneities of the ice properties (Dierking, 1999).

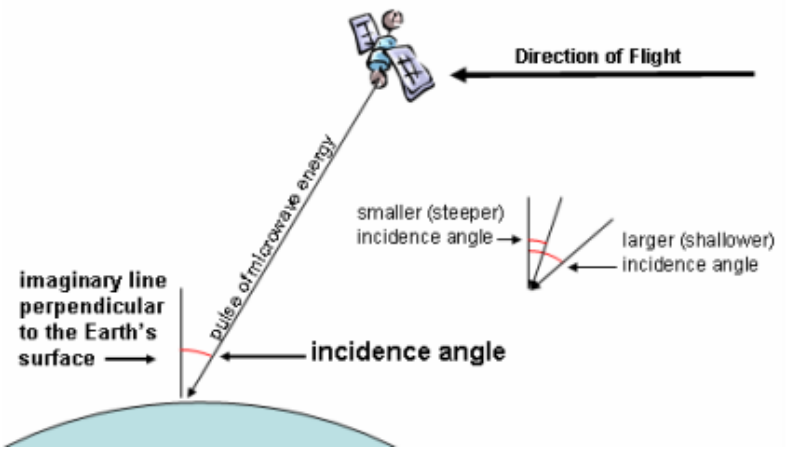

Figure 3.1. A simulation for the incidence angle of energy transmitted from a SAR sensor (adapted from Jensen, 2000).

3.2.3. Polarization

Polarization is another essential property when examining a target's microwave energy propagation and scattering. The polarization of an EM wave is defined by the orientations of the electric field vectors (Figure 3.2.). The incident and scattered waves can be measured using the same transmit and receive polarizations (called co-polarized, HH or VV), or they can be measured using perpendicular polarizations (called cross-polarized, HV or VH) (Richards 2009). Radar systems can have one, two or all four of these polarization combinations. Different types of radar systems are indicated in Table 3.2.

Table3.2. Different types of radar system polarization (adopted from the NRC website)

Type of Radar system	Polarization type
Single-polarized	HH or VV, there is possible to include HV or VH
Dual-polarized	HH and HV, VV and VH, or even HH and VV
Alternating polarization	HH and HV, alternating with VV and VH
Quadrature-polarization/ Polarimetric	Includes all HH, VV, HV, and VH

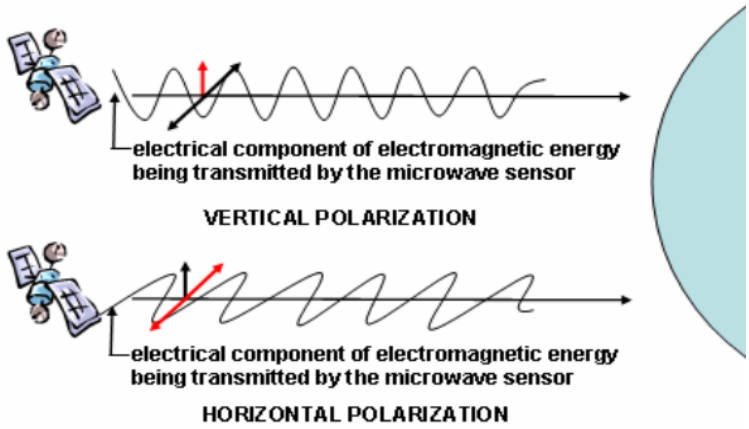

Figure 3.2. Polarization of incident EM energy where the same principal applies to returned energy. Microwave energy is emitted and received with a vertical (V) or horizontal (H) polarization (adapted from Jensen, 2000).

Many methods have been developed to discriminate between sea ice types and open water using different polarizations. The discrimination depends on the polarization difference, which refers to the difference in backscatter between, e.g., VV and HH, for the same surface feature. Typically, vertical waves have a greater transmission into the snow-covered sea ice at smooth interfaces relative to horizontal waves. Therefore, vertical waves have a greater opportunity to backscatter from the snow and ice volumes and brine inclusions in vertically oriented FYI. Although, when the brine volume in the snow cover is sufficiently large, the additional HH backscattering from the brine-wetted snow volume is greater than the VV backscatter from the sea ice volume. For example, new ice is better separated from young and first-year ice, or even intensity separation relative to some ice types, like brash, broken, and sizeable young ice, is largest at HH polarization (Dierking 2010a). As the snow-cover ages, the brine volume is reduced because of brine drainage and (or), during cold periods, freezing of water in the brine. Thus, brine volume is also reduced in low-salinity areas or where the snow cover is too thin to hold much brine, and the VV backscatter increases to overcome HH backscatter (Fujisaki-manome and Yamaguchi 2009).

Dual- and single-polarization SAR are widely used in operational sea ice monitoring to determine sea ice concentration and separate sea ice from open water (Moen et al., 2013). However, the area of deformed ice, level ice, and new ice can be well separated at single-polarization, while at cross-polarization, only deformed and level ice can be distinguished, and other ice types like thin ice cannot be discriminated because of too high noise level (Dierking 2010a). The HV channel was discovered to offer the greatest contrast between level and distorted FYI in subsequent investigations (M. P. Mäkynen et al. 2002; Wolfgang Dierking and Dall 2008; Gegiuc et al. 2018). However, the HV backscatter from level FYI can be extremely close to the SAR noise floor. As a measure of depolarization, the cross-polarization ratio, on the other hand, functions as an estimate and is predicted to rise with increasing roughness (Gill and Yackel 2012; Gill, Yackel, and Geldsetzer 2013; M. A. N. Moen et al. 2013; Fors et al. 2016). In dual-polarized SAR imagery with coincident VV and HH data, the discrimination of sea ice types and open water is based on both backscatter magnitudes and polarization differences (Nghiem and Bertoia 2001). Both cross-polarization ratios (VH/VV or HV/HH) can estimate depolarization (Oh, Sarabandi, and Ulaby 1992) related to sea ice surface roughness. As surface roughness is expected to be a vital contributor to depolarization of the SAR signal, the ratio of HV/HH increased with increasing surface roughness from snow-covered FYI (Moen et al. 2013; Brekke, Grahn, and Doulgeris 2015; Fors et al. 2016).

Overall, the use of multi-polarization combinations and ratios (polarimetry) is capable of distinguishing the surface roughness component of the scattering signature from the total observed scattering; thus, more detailed information about sea ice type and sea ice surface roughness could potentially be retrieved from high-resolution full-polarimetric SAR (M. Gupta et al. 2012; Nakamura et al. 2005; Gupta et al., 2012). Although the use of full-polarimetric

SAR is limited due to its small swath, the recent and future SAR missions that introduce compact polarimetry and full polarimetric scenes with wider swath width could change this (Fors et al. 2016).

It is difficult to quantify, estimate, and parameterize the physical surface roughness of sea ice using surface-based and remote sensing approaches, and it is also challenging to comprehend. However, thanks to satellite data, comprehensive datasets in the CAA and the surrounding Arctic environment may now be acquired. Therefore, the research presented in the next chapter uses satellite and aerial data to analyze surface roughness in the CAA and to estimate sea ice roughness using satellite data.

CHAPTER 4: Assessing RADARSAT Constellation Mission based sea ice surface topography retrievals using data from ICESat-2

4.1. Introduction

Sea ice topography is critical in climate modelling and marine navigation in Polar Regions. It is necessary for climate modelling as a boundary layer because of its effects on surface wind stress and determining aerodynamic roughness length (Lüpkes et al. 2012). Ice dynamics enhance topography and atmospheric boundary layer turbulence, affecting turbulent energy transfer and boundary layer height (Déry and Taylor 1996). The aerodynamic roughness length is reduced by the seasonal snow that tends to smooth the surface (Fassnacht, Williams, and Corrao 2009). The role of ice topography in ship navigation is related to relationships between different sea ice types, surface topography, ice thickness, and the dynamic processes divergence and convergence (Figure 2.1).

Sea ice surface roughness is a measurement of topography. It is created and increased by ocean-ice-air interactions, ice convergence, snow distribution, and ice surface melt (Rothrock and Thorndike 1980). The physical roughness of sea ice can be described by different horizontal and vertical parameters (Fors et al. 2016), which depend on the measurement direction and surface orientation (Hoffman and Krotkov 1989). The vertical measurement, considered primarily in sea ice studies, can be measured by taking the surface root-mean-square (S_{rms}) height, mean elevation, skewness, or kurtosis of the elevation profiles (Fors et al. 2016). The average variance of the surface topography around the mean is represented by the S_{rms} height (Saldern et al. 2005). The coefficient of variation, which is frequently used to refer to the ratio of S_{rms} height to mean elevation (e.g. Key and McLaren 1991; Goff et al. 1995), may be used to determine how the ice is deforming. The history of deformation for ice with a significant

coefficient of variation has consequently been more dynamic than that of ice with a modest coefficient of variation (Goff et al. 1995). The skewness is a metric for a distribution's asymmetry with respect to its mean, and the kurtosis quantifies how peaked or flat a distribution is in relation to another (Sachs 1992). The S_{rms} measurement is the most common method; however, the skewness and kurtosis method are even more sensitive to inhomogeneities and exhibit slightly lower correlations between SAR backscatter and laser altimeter measurement. In the study of different sea ice roughness measurements and their correlations with SAR backscatter during summer when melt ponds formed, the mean elevation measurement has similar results with S_{rms} and is more sensitive to heterogeneity, like sharp ridges, in the surface roughness sections (Fors et al. 2016). Ice roughness information can be obtained and analyzed through several remote sensing methods, including LiDAR, laser altimeter, photogrammetry, and SAR interferometry (Kwok 2014; Farrell et al. 2020). Among these techniques, SAR data meets all the requirements of operational planning because of its coverage independently of clear-sky conditions and light (Ulaby, Moore, and Fung 1986; Haas, Liu, and Martin 1999).

The Advanced Topographic Laser Altimeter System (ATLS) on IS-2 enables measurements of sea ice topography. The extraction of sea ice parameters from IS-2/ATLS data, such as surface roughness, ridge, leads and melt pond identification, and floe size distribution, is demonstrated by Farrell et al. 2020. Sampling every 0.7 m in the direction of flight, and with vertical height accuracy of 0.01 meters, IS-2 has substantially improved resolution over previous satellite altimeters, allowing researchers to quantify and determine the sea ice surface roughness and height in the Arctic (Duncan and Farrell, 2022). The minimal range of resolved sea ice features (average width of 7 meters) is one limitation of IS-2 based topographic measurement compared to wide-swath satellite imagery such as SAR (tens to hundreds of kilometres).

Recent advancements in C-band (4-8 GHz; wavelength 3.75-7.5 cm) SAR technology have increased data availability, for example, multiple along-orbit observations from the satellite constellations like RCM and Sentinel-1, including data in multi-polarization, compact polarimetric, and fully polarimetric formats. Utilizing polarimetric SAR has traditionally been limited due to its small area coverage. However, recent (e.g., RCM) and future SAR missions with compact and fully polarimetric capabilities over wider swath width will significantly enhance our ability to differentiate ice types, and the sea ice topography (i.e., surface roughness) component of the scattering signature from the total observed scattering (Nakamura et al. 2005; M. Gupta et al. 2012). This capability has been reconsidered in the context of retrieving sea ice topography regularly, at high spatial resolution (meter-scale), and over wide-swaths.

The frequent and all-season observation capabilities of RCM potentially allow for the estimation and evaluation of seasonal and spatial changes in sea ice topography. This chapter assesses RCM HH and HV polarization backscatter for the retrieval of surface roughness and, by proxy, information about sea ice thickness, using input IS-2 data for testing purposes. The following research objectives are addressed:

1- Describe the relationship between sea ice elevation (h) and surface roughness (both IS-2 width of height, width of height distribution (σ) and S_{rms}) as derived from IS-2 data.
2- Assess the inter-relationships between IS-2 laser altimeter-derived surface topography indicators (sea ice height and surface roughness) and RCM HH and HV backscatter measurements.
3- Evaluate the role of seasonal (environmental) changes, and SAR system (incidence angle) changes, in affecting the strength of IS-2 derived properties and RCM backscatter inter-relationships.

The first objective is motivated by the need to understand rudimentary thickness and roughness relationships for different study regions, here the CAA. The second and third objectives provide a practical means for assessing the drivers of C-band backscatter during winter and melt seasons and considering different incidence angles. A significant contribution from this research will be a methodology for the development of SAR-based maps of sea ice surface roughness over wider swaths, and potentially greater temporal frequency than IS-2.

4.2. Data and Methods

4.2.1. Study Area

This study collected data from two areas of landfast sea ice in the McClintock Channel in 2020 and 2021 [Figure 4.1]. This area is one of the biggest channels of the South-East part of the CAA. The CAA is covered in ice during the winter, both seasonal first-year landfast ice and MYI (Stewart et al. 2007). Since, the ice in this area is mainly seasonal landfast ice, the study of ice properties is less complicated (Maxwell 1981). Landfast ice refers to the sea ice linked to the coastline with a 100% ice concentration and moves very little or not at all (WMO 1970).

The McClintock channel has a mixture of FYI, deformed FYI, and MYI that is landfast for more than half the year until breaking up in late summer or early fall (Stewart et al. 2007; Haas and Howell 2015; Segal et al. 2020). The seasonal ice is maintained until breakdown begins in July, after which the waters refreeze in October (Melling 2002). There are no thin ice types by the end of March (Barber and Iacozza 2004). MYI has endured at least one summer's melt, whereas FYI expands and deteriorates seasonally. FYI is often no thicker than 2 m in the absence of ridging, but MYI can be approximately 3 to 4 m thick (Maykut and Untersteiner 1971).

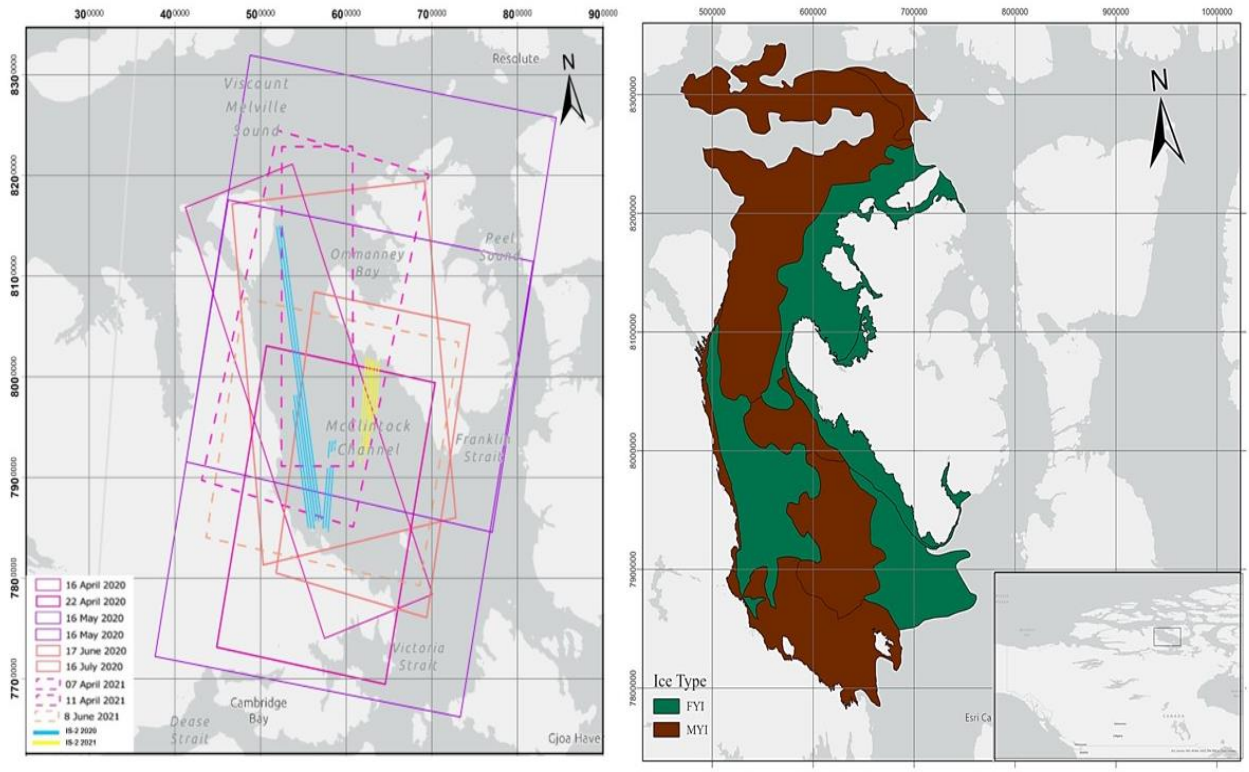

Figure 4.1. Left: Geographic map of study area, IS-2 data tracks, outlines of RCM image extents; Right: Ice types according to Canadian Ice Service weekly ice type maps of mid-April 2020.

4.2.2. Data Collection

Primary data for this study were collected during the winter period (April) through the melt season (June-July) in the years 2020 and 2021. Seven conventional dual polarized (HH and HV) RCM scenes with either medium resolution 50-meter or low resolution 100-meter pixel spacing, depending on acquisition mode, were acquired (Table 4.1.). Data from seven IS-2 ATL07 (sea ice surface elevation) tracks coincident with the RCM scenes were collected to examine the relationships of the height and roughness with the RCM backscatter (See Table 4.2.). Due to the nature of landfast ice, the sea ice is not significantly impacted by wind-driven movement after freeze-up and until break-up, hence the period under investigation (Melling 2002). The lack of

ice movements decreases the possible errors caused by the time difference between collecting data. As such, RCM and IS-2 data pairs from overpasses taken at different times can be analyzed without considering the ice movement.

The air temperature in this case study was around -22°C to -27°C during late winter, -7°C to -2°C during melt onset and 6°C to 10°C during the melt season. The air temperature was collected from the nearest Environment Canada stations (Cambridge Bay and Gateshead Island) located in the southwest and southeast portion of the study area from April 7th, 2020, to July 30th, 2021 (see Figure 4.2.).

Table 4.1. RCM image properties. The incidence angle is defined by the studied angle that corresponds to the location of the coincident IS-2 track passing within the RCM scene. See section 4.3.1 below for a description of how each season was delineated.

Date (yyyy/mm/dd)	**Time**	**Incidence Angle (°)**	**Mode**	**Season**
2020/04/16	08:02	22-26	100m Resolution 500km Swath A	Late Winter
2020/04/22	20:05	43-44	100m Resolution, 500km Swath A	Late Winter
2020/05/16	13:30	41-42	50m Resolution 350km Swath B	Late Winter
2020/06/17	15:10	42-44	50m Resolution, 350km Swath B	Melt
2020/07/16	16:29	22-24	100m Resolution 500km Swath A	Melt
2021/04/07	14:38	28-30	100m Resolution 500km Swath A	Late Winter
2021/06/08	13:37	39-40	50m Resolution 350km Swath B	Melt onset

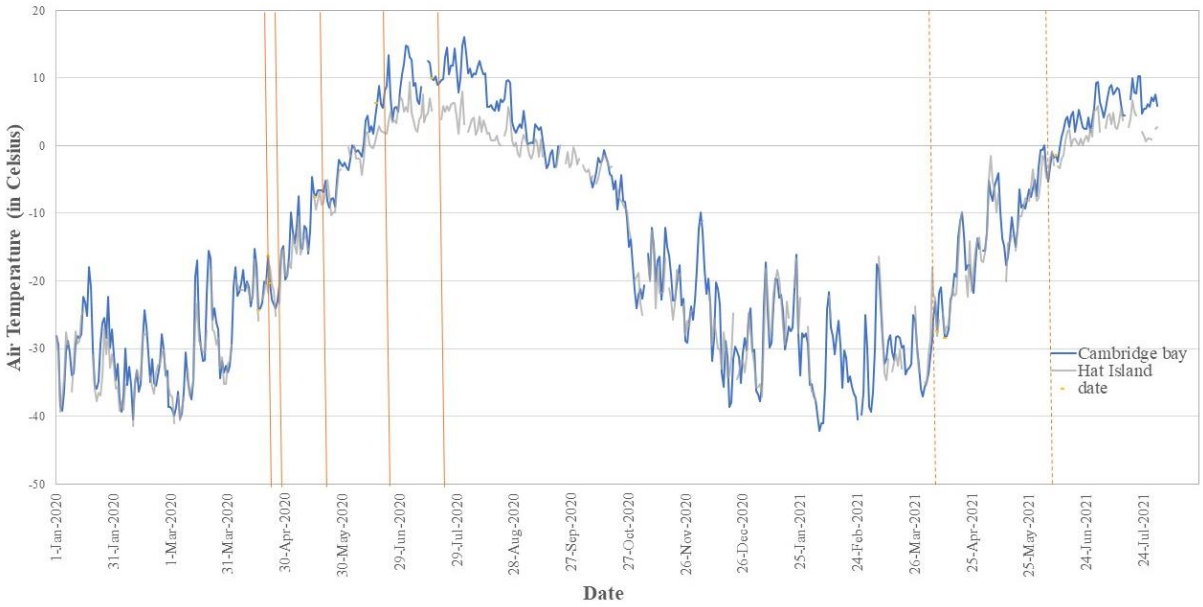

Figure 4.2. Plot of the progression of air temperature from January 1st, 2020, to July 30th, 2021, using data from the Environment Canada stations at Cambridge Bay (blue) and Gateshead Island (grey). Orange lines are the studied dates in 2020 (solid line) and 2021 (dashed line).

Table 4.2. Sea ice surface height (ATL07) IS-2 data tracks.

Date (yyyy/mm/dd)	**Strong Reference Ground Track**	**Start Time**	**End Time**
2020/04/16	Right	19:46	19:56
2020/04/22	Right	19:12	19:23
2020/05/16	Left	06:56	07:08
2020/06/17	Right	16:50	16:59
2020/07/16	Left	15:26	15:35
2021/04/07	Right	15:17	15:28
2021/06/08	Right	12:21	12:32

4.2.2.1. ATL07 IS-2 data

The sea ice elevation ATLAS (ATL07) from IS-2 data was collected from the National Snow and Ice Data Center (Table 4.2.). ATL07 is two-dimensional sea ice surface height distribution data used to delineate areas of sea ice surface types of individual height segments based on topography-related metrics like surface roughness. IS-2, launched in September 2018, can provide similar information about sea ice as airborne instrumentation, with notable differences in sensor resolution, sampling, and data processing techniques (see Figure 4.3.). The IS-2 platform was placed on a 91-day precise repeat orbit with a 92° inclination, enabling mapping to 88° latitude in both the Northern and Southern Hemispheres (Kwok et al., 2019). The central Reference Pair Tracks show with RPT, where follows the Reference Ground Track (RGT). RGTs match the nadir tracks of the predicted 1,387 orbits and related spacecraft ground tracks corresponding to each repeat cycle (Kwok et al., 2019). GTNXs are the ground tracks generated by successive ATLS spots (green circles), where N is the number of beam pairs (1-3), and X is the beam side left (L) or right (R) (see Figure 4.3.). Two beams are separated by about 90m in each pair, and each pair consists of a strong energy beam and a low energy beam.

ATL07 contains profiles of sea surface/sea ice heights and surface type of individual height segments along each of the six ground tracks (Kwok et al. 2019). To identify ice types, each height segment in ATL07 is assigned as a surface type (e.g., smooth, medium, and rough ice). The primary usage of surface types with local height statistics is to determine the suitability of a given height segment to use as a sea surface height sample in detecting leads and sail heights (Kwok et al. 2019).

Individual ATL07 height estimations are produced from height distributions derived from 150 geolocated photons from the ATLS Global Geolocated Photon Data package (Neumann et

al. 2019). The ground distance travelled by the pulse footprints determines the variable along-track length of a height segment (Ls) associated with a height estimate. Particularly the Ls is equal to the multiplication of the number of pulses and interpulse distance, where this length varies with surface reflectance. Note, approximately 0.7 meters separates each pulse. The 150-photon aggregates were chosen to offer a 2 cm height precision over mainly flat surfaces. Strong beam height segments (Ls) range from 10 to 200 m in length, whereas weak beam height segments (Ls) range from 40 to 800 m. The segment length (rs = Ls+f) and the beam footprint dimension (f ~ 17 m) must be combined to get the spatial resolution.

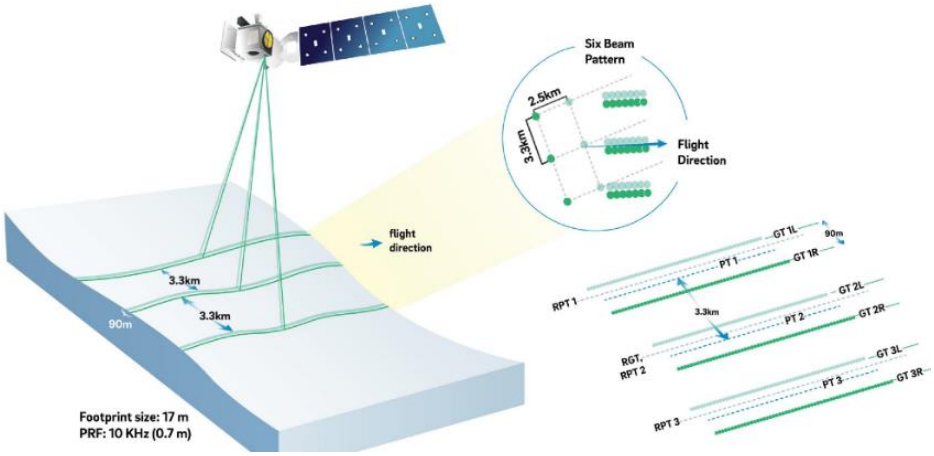

Figure 4.3. Schematic of ATLS 6-beam pattern, from Smith et al. 2019. The beams are weak (lighter colour) and strong (darker) for each side, where that side can be opposite in reverse direction. The track pairs (GT1, GT2, and GT3) are always numbered from left to right with the direction of travel; however, the beam numbers and beam strengths weak and strong), fixed to the ATLS instrument, remain constant regardless of the system's orientation.

All heights in ATL07 are referenced to the WGS84 ellipsoid, but the ocean tides, solid earth tides, load tides, solid earth pole tides, inverted barometer effect, and mean sea surface have been subtracted (Kwok et al. 2019). The statistics mean height ($\bar{h}$) and standard deviation (σ) of heights are calculated as follows:

$$\bar{h} = \frac{\sum_N L_s^i h_s^i}{\sum_N L_s^i} \quad [3] \qquad \sigma = \frac{\sum_N L_s^i (h_s^i)^2}{\sum_N L_s^i} - \bar{h}^2 \quad [4]$$

The heights are weighted by the corresponding length of individual height segments (*L*s), and *N* is the number of segments (Kwok et al. 2019). Sea ice heights are only estimated when the gridded Multi-sensor Analyzed Sea Ice Extent (MASIE) product derived local sea ice concentration is >15% (Fetterer et al. 2010).

In this case study, two indicators of surface roughness have been analyzed: (1) the standard deviation (σ) of ATL07 sea ice height segments, known as the width of height distribution, and (2) the S_{rms} derived from a collection of output GT height values within an image segment i.e. object (see description below). The resulting dataset is of surface elevation and roughness profiles (Farrell et al., 2020).

4.2.2.2.SAR imagery

RCM satellites have a ground swath of about 350km or 500km, depending on acquisition mode, which enables comprehensive area monitoring of maritime approaches of Canada on a daily basis and improved hazard monitoring (De Lisle and Iris 2018). At low resolution mode the RCM data includes HH and HV channels that has 32 and 82 m range and azimuth resolutions and is therefore resampled to square 100m by 100m pixels in the final image product (Dabboor, Montpetit, and Howell 2018).

The SAR images were collected during winter 2020 and 2021 showed low to high incidence angles. The two RCM images for melt-onset stage have a high incidence angle. Additional RCM images with high and low incidence angles in 2021 were studied (See Table 4.1.).

4.2.3. Data Analysis

According to the flowchart in Figure 4.4., the IS-2 dataset and RCM images were processed to enable the inter-comparison of IS-2 ATL07 derived variables and SAR-based variables. To summarize:

i. RCM images were pre-processed to retrieve calibrated HH and HV polarization backscatter, band math, and GLCM texture parameters;

ii. A winter RCM image from each year 2020 and 2021 was also segmented into image objects representing homogeneous sea ice features;

iii. Image objects were labeled as ice type FYI or MYI and validated using Canadian Ice Service stage of development (ice type) maps used for operational purposes (see Figure 4.5.);

iv. IS-2 ATL07 datasets were used to quantify surface roughness and sea ice height; and

v. Image objects were reduced to widths corresponding to the IS-2 swath and used to combine the IS-2 and RCM derived data based on ice type, varying the object widths, seasonal changes, and RCM incidence angles.

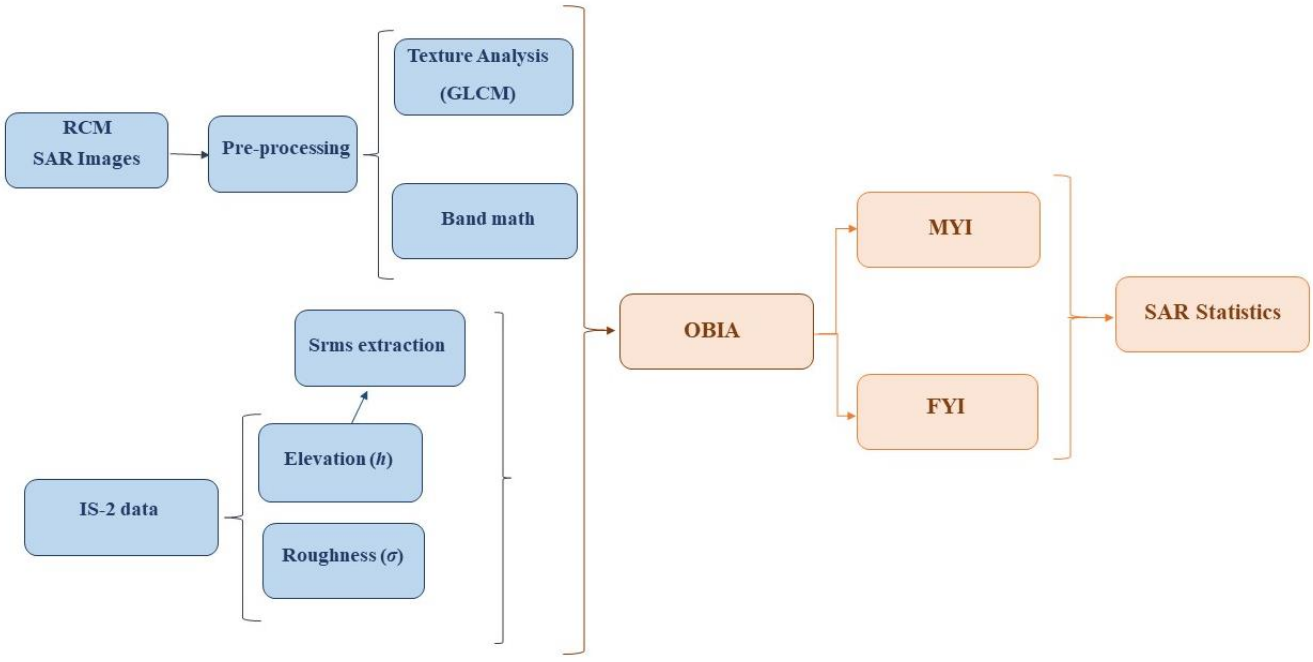

Figure 4.4. Flowchart for the RCM and IS-2 data analysis

In order to maintain consistency, each SAR image was radiometrically calibrated to sigma-nought, thermally noise-removed, and then a Lee speckle filter with a 7 x 7 window was used to decrease image speckle and preserve the specific signal information (Lee 1986). The noise estimate values from the annotation dataset for each RCM product were subtracted to remove thermal noise. Bilinear resampling was used to transform the images into a Universal Transverse Mercator (UTM)/WGS-84 projection, with 40 m pixel spacing. Outliers were eliminated to maintain a consistent quantization to 64 grey levels for grey-level co-occurrence matrix (GLCM) computations because texture parameters are affected by extreme values. Outlier HH values more than 0.3 (5.2 dB) were truncated to 0.3, while all values less than 0.0001 (40 dB) were truncated to 0.0001 (Scharien and Nasonova 2020).

A set of GLCM-based texture parameters were derived from each backscatter channel, following the derivations provided by Scharien and Nasonova (2020). The parameters in each GLCM grouping are correlated (Hall-Beyer 2017). As such, only one parameter from each of the main GLCM groupings was selected, including Contrast (CON), Angular Second Moment (ASM), and GLCM Correlation (GLC) (See Table 4.3.).

Table 4. 3. The GLCM statistics are based on co-occurrence texture. Where, C_{ij} is the co-occurrence probability between row and column grey levels i and j, and μ_i, μ_j, σ_i and σ_j are respectively means and standard deviations (adapted from Scharien and Nasonova 2020).

Parameter	Derivation
CON	$\sum C_{ij}\,(i-j)^2$
ASM	$\sum {C_{ij}}^2$
GLC	$\sum C_{ij}\left[(i-\mu_i)(j-\mu_j)/\sqrt{(\sigma_i^2)(\sigma_j^2)}\right]$

In total, the RCM dataset from each image, resulted in 12 bands:

- Calibrated backscatter (2): HH and HV;
- Backscatter sums and differences (2): HH+HV, HH-HV;
- Backscatter ratio and multiple (2): HH/HV, HH*HV; and
- Band-wise GLCM texture parameters (6): HH $_{CON}$, HH$_{AMS}$, HH$_{GLC}$; HV $_{CON}$, HV$_{AMS}$, HV$_{GLC}$.

These 12 bands were assessed in power format. In addition, the first six bands were converted to dB to consider a more comprehensive analysis.

There is limited information available on the application of segment-based i.e., object-based image analysis (OBIA) for optimizing the use of multi-polarization C-band SAR for detecting sea ice topography. This project addressed this issue, by applying an OBIA framework to extract RCM and IS-2 statistics from spatially coincident RCM/IS-2 pairs. An OBIA enables the inter-comparison of RCM derived backscatter and texture, and IS-2 topography information, for homogeneous image areas corresponding to discrete ice types.

In order to apply OBIA, the HH channel of each winter SAR image was thermally noise-removed, radiometrically calibrated to sigma-nought, and then a median 3 x 3 speckle filter was applied. Median filtering is a nonlinear technique that eliminates noise while maintaining edges (Raju, Maul, and Bargiela 2015). In addition, it has been proven that median filtering is a trustworthy technique for eliminating impulsive noise without impairing edge details (Pitas and Venetsanopoulos, 1993). The Geomatica 2017 image-segmentation algorithm was used to delineate homogenous regions based on statistical region-growing, with shape, colour, and scale criteria optimized for delineating sea ice objects representing homogeneous ice classes. The segmented objects were then manually labelled according to their dominant ice class, as

appearing in the RCM images used to create the objects. Canadian Ice Services weekly ice charts were also used to guide the segment labelling (See Figure 4.5.).

In order to compare IS-2 data with the RCM backscatter, two buffer distances (20-meter and 40-meter) were applied over the along-track IS-2. A shorter buffer distance typically results in lesser discrepancies between IS-2 and RCM. A smaller distance is not providing enough overlapped satellite number of pixel to depict accurately the ice elevation and roughness change. Therefore, in this study, a larger buffer distance was analyzed and results from that analysis are shown from here-on.

Within the study region, 77726 objects were generated for the 2020 dataset and 8355 objects for 2021 dataset. The object dataset was reduced to those spatially coincident to IS-2 tracks. This resulted in 2221 objects during both 2020 and 2021 winters, an average of 289 during melt onset, and 519 objects during the melt season. These objects have an average area of 62.89 km^2 during winters, 14.52 km^2 during melt onsets, and 14.93 km^2 during the melt season.

The object-wise mean h, σ, and S_{rms} values were extracted. The minimum, maximum, mean, range, and standard deviation of the backscatter statistics were computed from the intensity values. As a result, the average RCM pixel counts sampled per image object was 75, ranging from 25 to 107 pixels. The average IS-2 data points were 146 per image object ranging from 49 to 169.

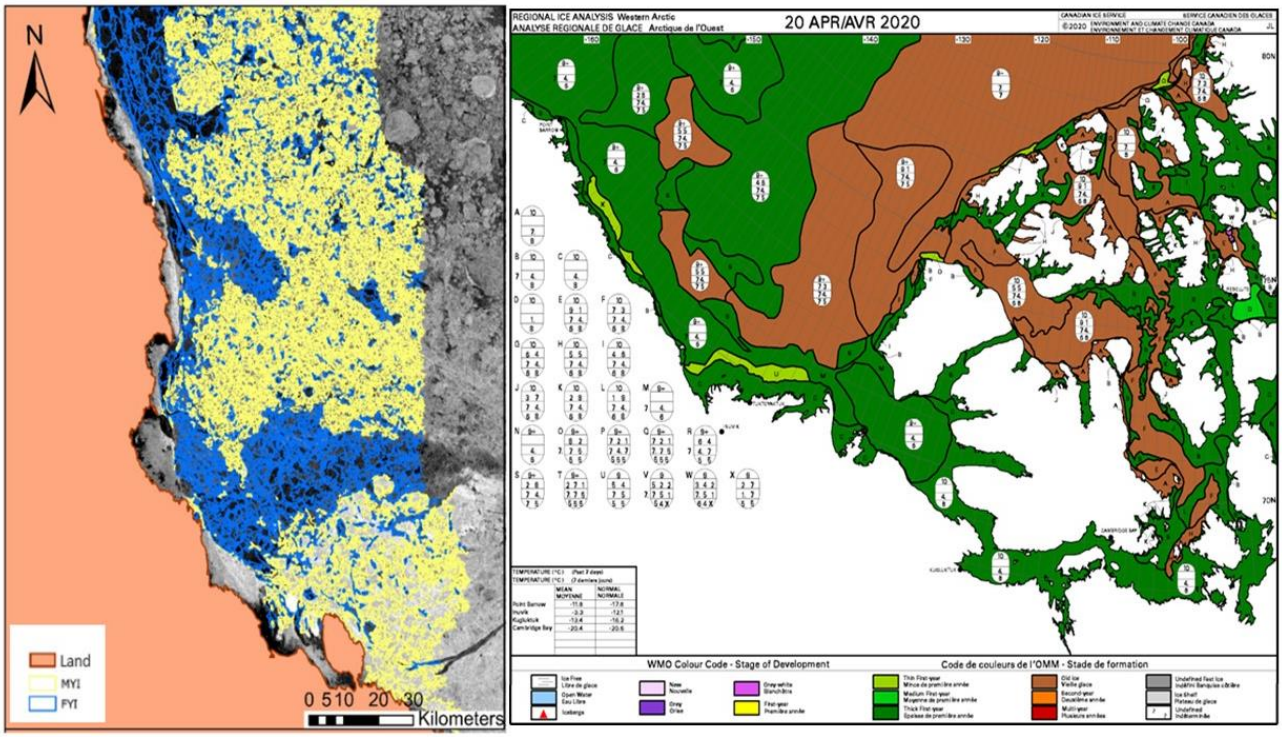

Figure 4.5. Left: extracted segments from the HH channel on April 22nd, 2020. The segments are labelled based on the ice type. Right: Canadian Ice Service ice chart related to the same week.

Bivariate relationships between RCM backscatter and GLCM parameters, and IS-2 parameters were assessed using Pearson's correlation coefficients (*r*). The strength of a linear relationship between two variables are measured by *r*, which ranges from -1 to +1, and a p-value is used to assess statistical significance. It must only be applied when the underlying assumptions are met. In addition to *r* assessment, SAR backscatter was used as the independent variable in a regression analysis using ordinary least squares (OLS), and *h* was used as the dependent variable. A linear function was fitted to *h* and backscatter for the OLS.

This study and prospective relationships between RCM backscatter and sea ice topography touch seasonal changes, radar incidence angle, polarization, and texture (GLCM). All the relationships are assessed considering SAR images in power and dB formats and differentiating

ice types. The GLCM results are not shown due to poor overall relationships between texture and IS-2 derived parameters.

4.3. Results

Object-wise mean values of along-track, IS-2 derived, surface parameters h, S_{rms}, and σ are shown in Figures 4.6. - 4.8. The average h range is -0.4 m to 0.93 m, S_{rms} is 0.015 m to 0.5 m, and σ is 0.09 m to 0.46 m. As anticipated, MYI has the highest h (0.93 m), and the smallest h (-0.4 m) is detected in the melt season. FYI has a lower average S_{rms} (~ 0.09m), while MYI showed the highest average S_{rms} (~ 0.46 m). Due to S_{rms} being calculated from h, their distributions are similar as expected. Due to atmospheric forward scattering from clouds, there are evidence for a negative elevation bias on melt season tracks. The degree of atmospheric forward scattering, which expands the waveform and results in an incorrectly calculated elevation, depends on clouds optical depth, height, vertical extent, and particle size depth, height, vertical extent, and particle size of the clouds (National Snow and Ice Data Center 2009). The negative bias also happens when the energy of collecting data is low laser transmitted energy or the collected photons are low (Borsa, Fricker, and Brunt 2019). Due to the fact that the photon distance measurements are not given in sequential along-track distance order, this might lead to incorrect behaviour, including, in some circumstances, negative segment lengths (Petty and Kwok 2020). Using Moderate Resolution Imaging Spectroradiometer (MODIS) images to check the circumstances of the area during the IS-2 data collection, the existence of clouds were observed, as along with inconsistency for the IS-2 along track data, during melt season.

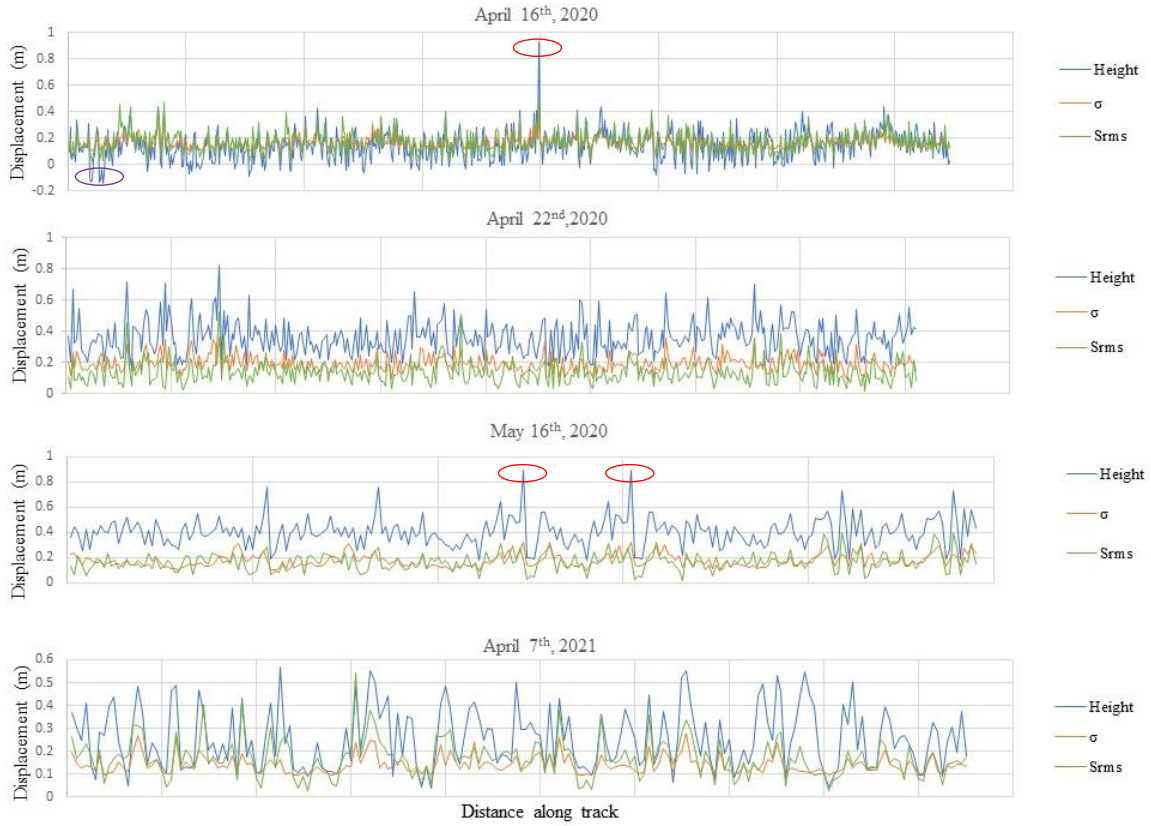

Figure 4.6. Along-track profiles of object-wise mean values of IS-derived surface parameters *h*, *σ*, S_{rms} during winter 2020 and 2021. The red circle is showing a thicker MYI area. The purple circle is the FYI area between MYI and Stefansson Island. The distance along track is ~284.7 km (April 16th, 2020), ~157.3 km (April 22nd, 2020), ~59.61km (May 16th, 2020), and ~ 86.93km (April 7th, 2021).

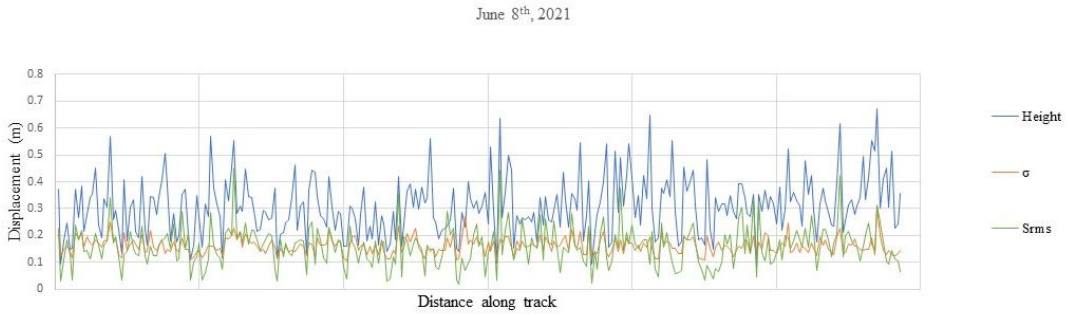

Figure 4.7. Along-track profiles of object-wise mean values of IS-derived surface parameters *h*, σ, S_{rms} during melt-onset 2020 and 2021. The red circle is showing a thicker MYI area. The distance along track is ~ 105.18km (June 8th, 2021).

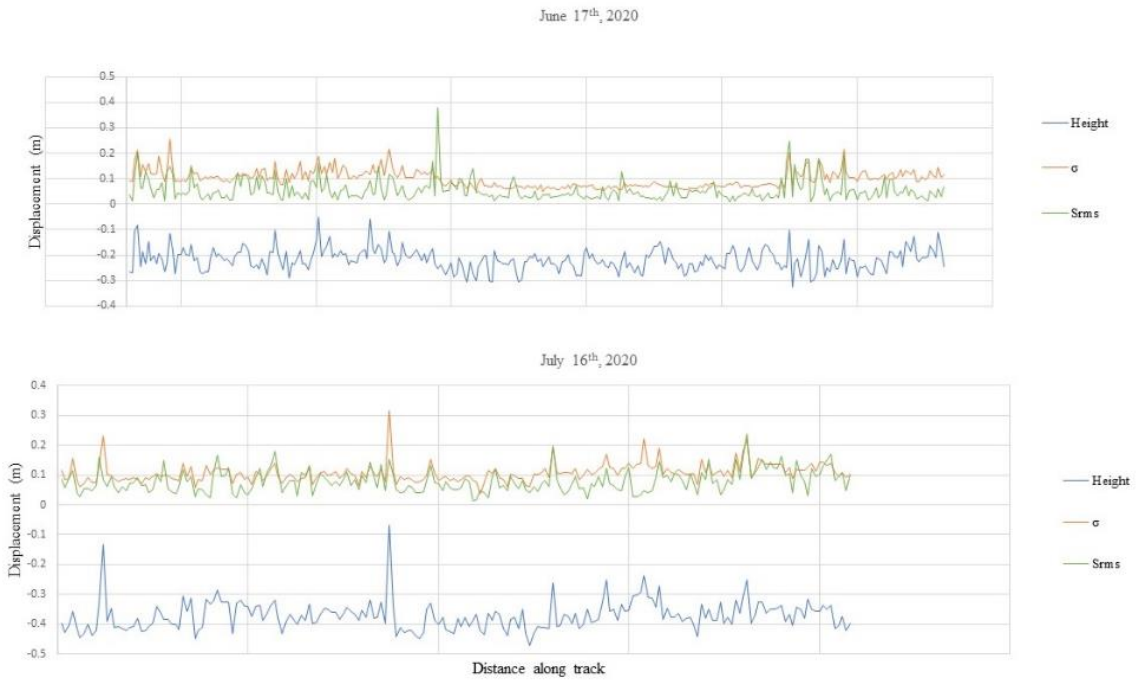

Figure 4.8.Along-track profiles of object-wise mean values of IS-derived surface parameters *h, σ, S_{rms}* during melt season 2020. The distance along track is ~133.83km (June 17th, 2020) ~101.17km (July 16th, 2020).

The frequency distributions of along-track, IS-2 derived, surface parameters *h*, S_{rms}, and *σ* are shown in Figures 4.9.- 4.10. In terms of seasonal changes, the distribution of MYI *h* shows a normal distribution during winter and melt-onset period. The FYI *h* and MYI *h* during melt season show a bimodal distribution. The FYI *σ*, S_{rms}, and MYI *σ* and S_{rms} plots have positively skewed distributions for the all seasons.

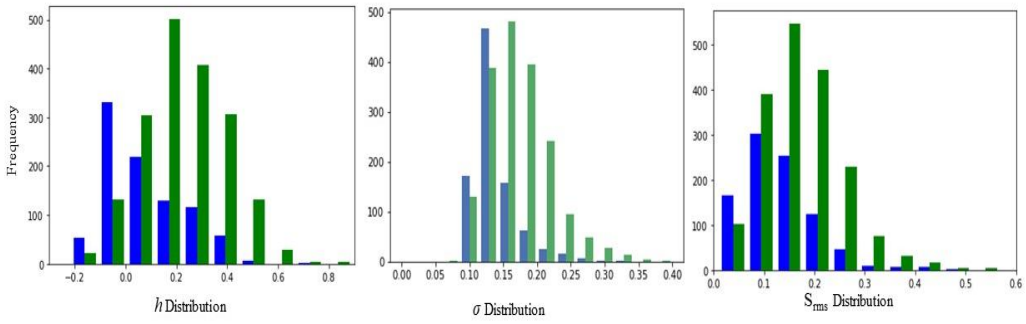

Figure 4.9. Distributions of IS-2 derived *h* [left], *σ* [middle], and S_{rms} [right] during winter. FYI is shown in blue, and MYI in Green.

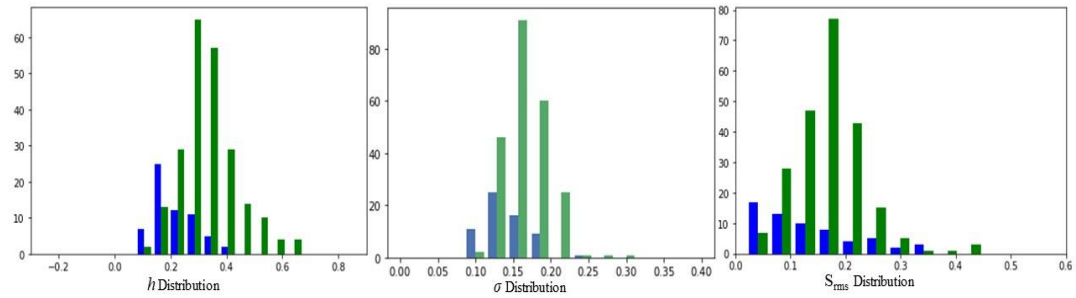

Figure 4.10. Distributions of IS-2 derived h [left], σ [middle], and S_{rms} [right] during melt-onset. FYI is shown in blue, and MYI in Green.

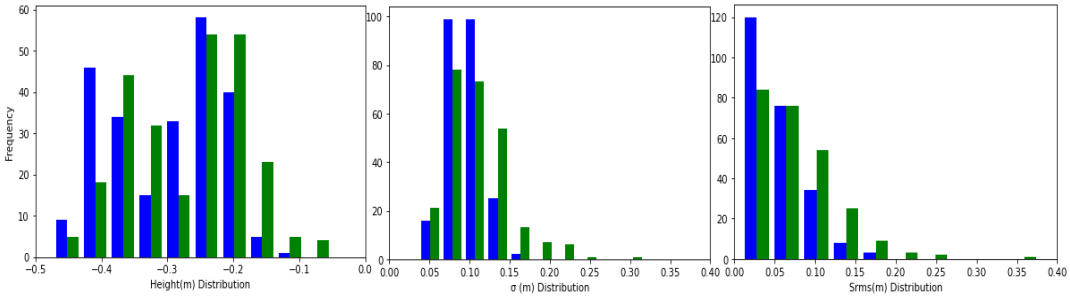

Figure 4.11. Distributions of IS-2 derived h [left], σ [middle], and S_{rms} [right] during melt season. FYI is shown in blue, and MYI in Green.

Linear OLS models and relationships between IS-2 derived h and σ are seen in Figures 4.12-4.13. The relationship between h and S_{rms} showed a lower correlation than the relationship between h and σ. However, h and σ are strongly positively correlated (p-value = 0.0). The correlation between h and σ during winter (r ~ 0.7 to ~ 0.8) is higher than melt onset and melt season (r ~0.4 to ~0.6). This supports the hypothesis that dynamic deformation mechanisms (e.g., ridging) regulate the development of mean late-winter thickness, especially in FYI, because level ice is subject to the same growing conditions throughout the winter and has a nearly constant thickness as a result (Peterson, Prinsenberg, and Holladay 2008). FYI during winter showed a higher R^2 with an average of 0.69 for the three winter cases.The highest FYI R^2 is observed during late April (~0.75). Note, the R^2 during melt-onset and melt period is not

showing consistant results due to the highly variable surface conditions (e.g., melt ponds and wet snow).

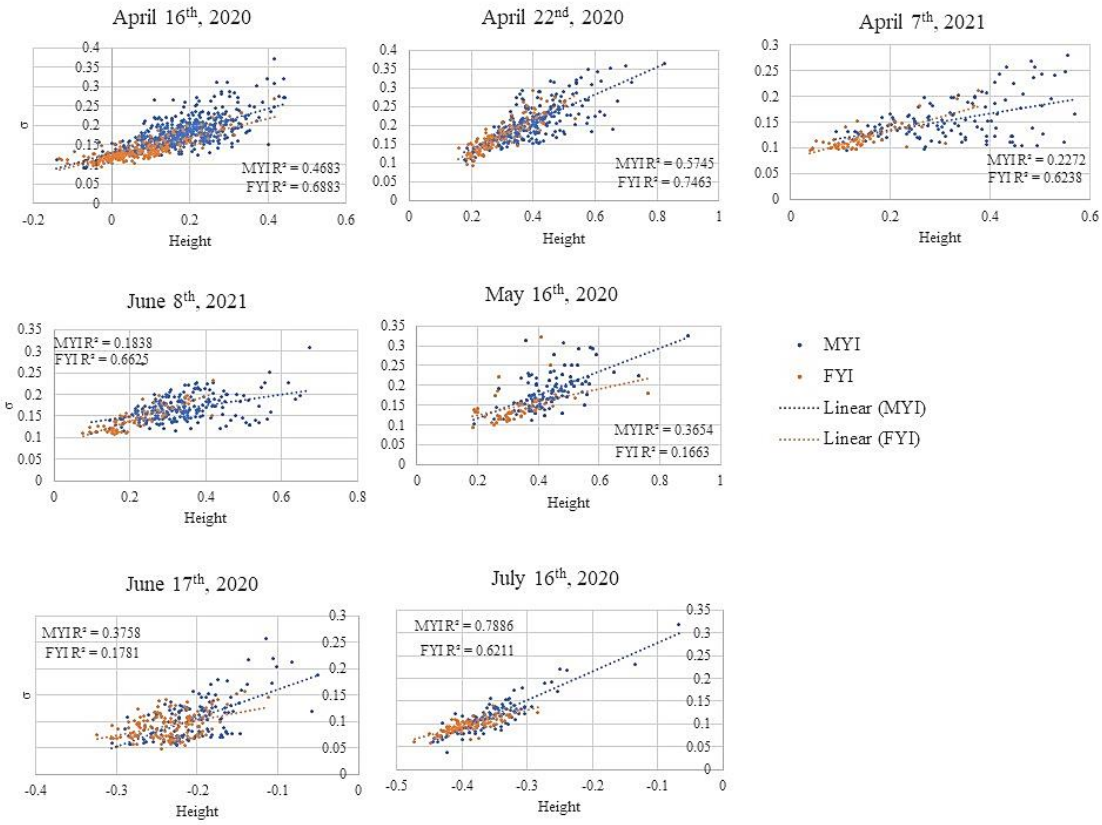

Figure 4.12. Linear OLS model and relationships between IS-2 derived σ (y) and h (x) for all dates. MYI is shown in blue, and FYI in orange.

4.3.1. Advanced Scatterometer on MetOp-A (AScat) backscatter time series

The seasonal evolution of Advanced Scatterometer (AScat) backscatter in VV polarization over the study area has been analyzed to situate the data in a seasonal context (i.e., winter, melt onset, and melt) (see Figure 4.13.). The AScat has a 5.25 GHz frequency, 4.45 km resolution, and an incidence angle is 40°. FYI and MYI ice-type difference is evident during winter, where MYI has higher backscatter than FYI. However, the separability of MYI and FYI is challenging during melt onset, when FYI and MYI backscatter first converges, and melt season, typically

starting in early June, when the there is variability in backscatter denoting the transition from melt onset to melt season.

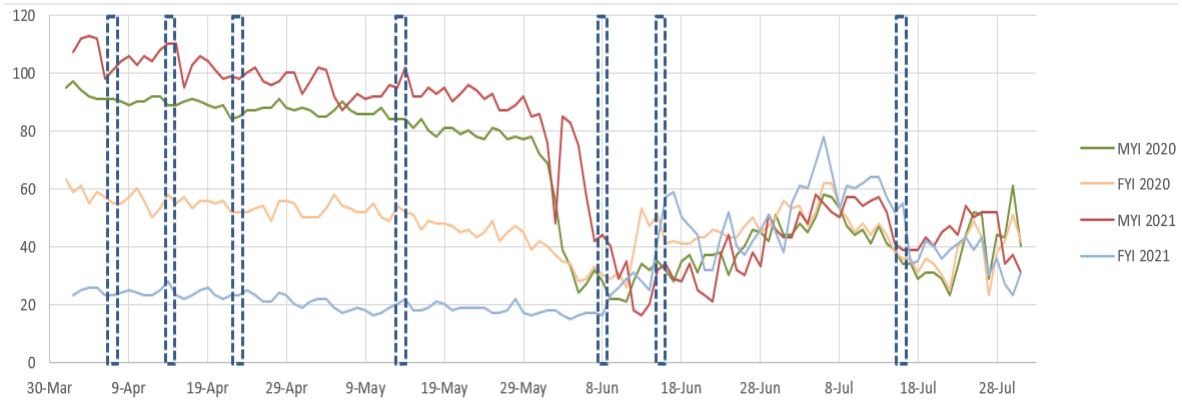

Figure 4.13. ASCAT backscatter time series over McClintock Channel from 1 April to 31 July in 2020 and 2021. Dashed boxes showing the studied dates.

4.3.2. RCM and IS-2 relationships during winter

The strongest correlation coefficients between IS-2 parameters (h, σ and S_{rms}) and examined RCM parameters for winter are given in Table 4.4, and the corresponding RCM bands are in Table 4.5. The correlation between h and backscatter is predominantly stronger than it is for the roughness related parameters and backscatter. In addition, the correlation between backscatter and σ is stronger than the correlation between backscatter and S_{rms}.

In this study, three ranges of low, moderate, and high incidence angles during winter have been assessed. The range of low incidence angle range is 20° to 26°, the moderate range is between 28° to 42°, and the high incidence angle is 43° to 50°. The effect of the incidence angle on the relationships in Tables 4.4 and 4.5 is apparent. Regarding backscatter coefficients, all incidence angle ranges (low, moderate, and high) show strong correlations between h and backscatter, with a stronger relationship observed for FYI compared to MYI at the low incidence angle range. At the high incidence angle range, the backscatter and h is more strongly correlated

for MYI than FYI. In terms of the relationships between backscatter and surface roughness at different incidence angles, the parameter σ at moderate incidence angle shows the strongest correlation compared to *h*, for FYI.

In terms of strongest correlated RCM bands, the HH+HV, HH, and HV are the most common bands that show potential suitability for winter sea ice topography retrieval. Figure 4.14. shows the linear relationships between these bands and *h* for both MYI and FYI during winter 2020. From the April 16th comparison, 55% of the variation in FYI *h* can be explained by HH+HV and HH, whereas it is 26% of the variation in *h* explained by HV. Regarding MYI, 43% of variation in *h* is explained by HH+HV and HH, and 28% with HV polarization. From the April 22nd comparison, 26% of the variation in FYI *h* can be explained by HH, or 25% by HH+HV, or 19% by HV. Regarding MYI, 55% of variation in *h* is explained by HH+HV and HH, 50% by HV.

Table 4.4. *r* between IS-2 *h*, σ, and $S_{rms,}$ and RCM backscatter coefficients in dB and power format during winter. Correlations are presented according to MYI and FYI samples. Correlations more significant than 0.6 are bolded.

	dB			Power			
	h	σ	S_{rms}	*h*	σ	S_{rms}	Objects number
22°-24°	April 16th, 2020						
FYI	**0.732**	0.568	0.593	**0.743**	0.582	**0.600**	221
MYI	**0.636**	0.463	0.295	**0.612**	0.440	0.277	525
43°-44°	April 22nd, 2020						
FYI	0.543	0.432	0.230	0.506	0.374	0.523	115
MYI	**0.712**	**0.536**	0.327	**0.744**	0.530	0.403	283
41°-42°	May 16th, 2020						
FYI	**0.714**	0.438	0.481	**0.749**	0.375	0.393	77
MYI	0.197	0.109	-0.111	0.173	0.073	-0.148	168
28°-30°	April 7th, 2021						
FYI	0.566	**0.668**	0.548	0.597	**0.693**	0.520	62
MYI	**0.721**	0.132	0.182	**0.710**	0.086	0.170	128

Table 4.5. Highest correlated bands with IS-2 derived *h*, σ, and S_{rms}.

	dB			Power		
	h	σ	S_{rms}	*h*	σ	S_{rms}
22º-24º	April 16th, 2020					
FYI	HH	HH+HV	HH+HV	HH	HH+HV	HH+HV
MYI	HH+HV	HH	HH	HH+HV	HH	HH
43º-44º	April 22nd, 2020					
FYI	HH+HV	HH	HH	HH	HH	HH
MYI	HH+HV	HV	HV	HH+HV	HV	HV
41º-42º	May 16th, 2020					
FYI	HH-HV	HH*HV	HH+HV	HH-HV	HH	HH+HV
MYI	HH-HV	HH-HV	HH	HH-HV	HH-HV	HH
28º-30º	April 7th, 2021					
FYI	HH+HV	HH+HV	HH+HV	HH+HV	HH+HV	HH+HV
MYI	HV	HV	HV	HV	HV	HV

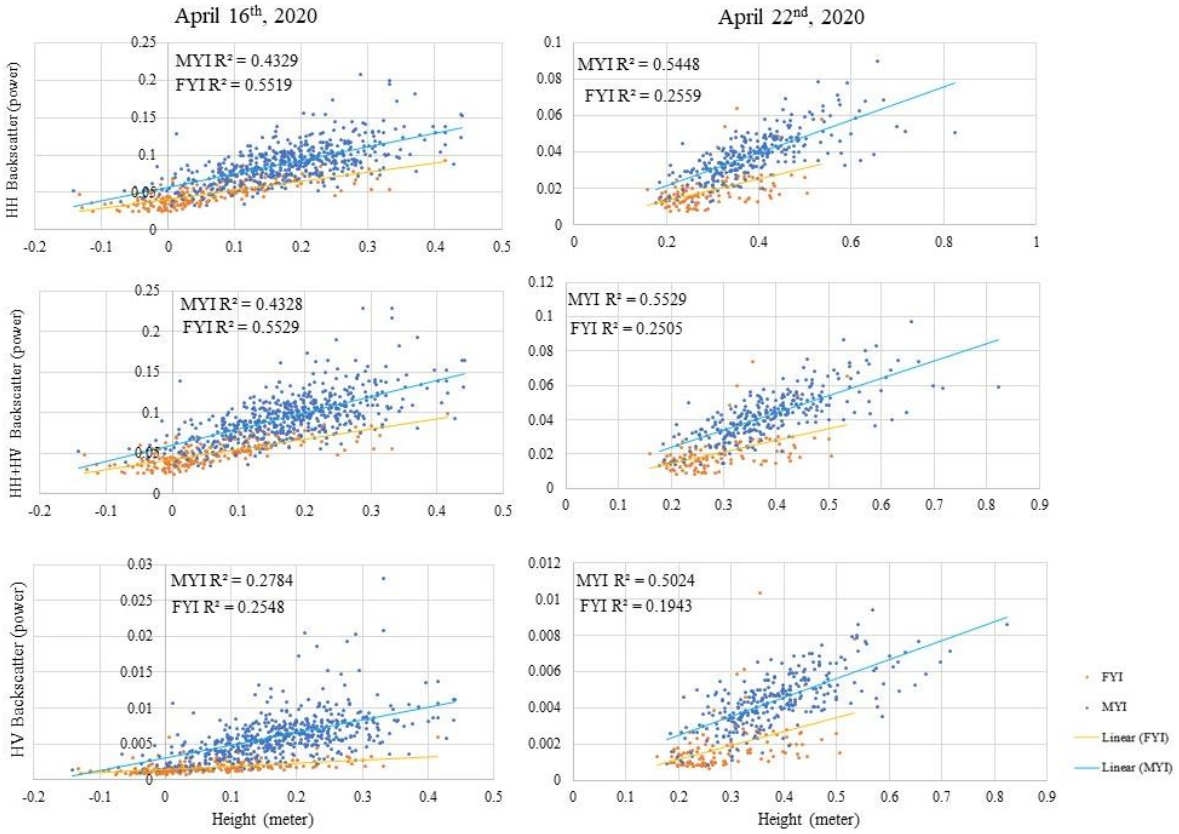

Figure 4.14. Linear OLS models of the highest correlated backscatter bands and *h*, for winter RCM scenes.

4.3.3. RCM and IS-2 relationships during melt onset

The strongest correlation coefficients between IS-2 parameters (*h*, σ and S_{rms}) and examined RCM parameters for melt onset are given in Table 4.6, and the corresponding RCM bands are in Table 4.7. Similar to the winter correlation results, correlation between *h* and backscatter is consistently stronger than it is for the roughness parameters and backscatter. The highest correlation is for MYI *h* and HH+HV ($r \sim 0.69$), which is pretty similar in terms of correlation strength to winter results. The HH and HH+HV bands show the most potential for surface topography retrieval during melt onset.

Table 4.6. *r* between IS-2 *h*, σ, and $S_{rms,}$ and backscatter parameters in dB and power format during melt-onset. Correlations are presented according to MYI and FYI samples. Correlations more significant than 0.6 are bolded.

	dB			Power			
	h	σ	S_{rms}	*h*	σ	S_{rms}	Objects number
39°-40°	June 8th, 2021						
FYI	**0.644**	0.548	**0.627**	**0.637**	0.456	0.557	62
MYI	**0.693**	0.163	0.142	**0.694**	0.063	0.141	227

Table 4.7. Highest correlated RCM bands with ice *h*, σ, and S_{rms}.

	dB			Power		
	h	σ	S_{rms}	*h*	σ	S_{rms}
39°-40°	June 8th, 2021					
FYI	HH+HV	HH	HH	HH	HH-HV	HH
MYI	HH+HV	HV	HV	HH+HV	HV	HV

4.3.4. RCM and IS-2 relationships during melt season

The strongest correlation coefficients between IS-2 parameters (*h*, σ and S_{rms}) and examined RCM parameters for the melt season appear in Table 4.8. Due to low correlation, corresponding

RCM bands are not shown, as they were for winter and melt onset. Regarding the ASCAT analysis (section 4.3.1), the separability of FYI and MYI near the June 17th acquisition is smaller than it is during the July 16th acquisition. As anticipated, there are no notable correlations associated with the June 17th acquisition, which occurred after surface flooding, i.e., formation of surface melt ponds from melting snow and ice. Therefore, finding the most correlated bands for June 17th is not possible. In the case of July 16th, there are notably stronger correlations between *h* and RCM backscatter for FYI than for MYI. During this period, surface melt ponds have typically drained from permeable FYI whereas they can remain on MYI.

Table 4.8. r between IS-2 h, σ, and S_{rms}, and RCM backscatter coefficients in dB and power format during melt season. Correlations are presented according to MYI and FYI samples.

	dB			Power			
	h	σ	S_{rms}	h	σ	S_{rms}	Objects number
42°-44°	June 17th, 2020						
FYI	-0.327	0.269	0.063	-0.352	0.266	0.084	140
MYI	-0.083	0.199	-0.085	-0.069	0.215	-0.046	147
33°-35°	July 16th, 2020						
FYI	0.497	0.325	0.250	0.512	0.352	0.245	101
MYI	0.021	0.126	0.245	0.005	0.106	0.250	107

4.4. Discussion

The results in Section 4.3 revealed two recurring behaviours. First, the IS-2 and RCM comparisons made during melt-onset and melt were consistently poorer, in terms of correlations, than those made during the winter. Second, taking into account the correlations between IS-2 and RCM during winter, incidence angle plays a significant role. This section discusses the variability of the links between sea ice properties and RCM parameters and the impact of the incidence angle on sea ice elevation readings.

4.4.1. IS-2 properties and their inter-relationships

Generally, the results of this study demonstrate that IS-2 ATL07 can be a reliable tool to measure sea ice elevation and roughness during winter, whereas it does not appear to give realistic elevation and, likely, derived roughness information, during the melt period. Two issues lead to uncertain absolute elevation values for this region. First, there are few open water areas from which to reference sea level and, second, snow may be penetrated by the ICESat-2 green laser's (532 nm) wavelength (Harding et al. 2015), resulting in an inaccurate total freeboard measurement (Yang 2020).

Sea ice elevation can be an indicator of LKFs, specifically ridges, based on a threshold. Based on Petty and colleagues (2016), there are two thresholds for ridge sails, 0.2 m (small sails) and 0.8 m (large sails). However, sail heights are markedly higher (~1.5–1.7 m) over CAA (A. A. Petty et al. 2016), so that the threshold of 0.8m applies to data in this study. The features over 0.8 m showed the edge of FYI and MYI area (Figure 4.6. and Figure 4.7.).

The sea ice surface roughness in this study was measured using two methods, σ and S_{rms}. The S_{rms} is commonly used in order to measure sea ice roughness quantitively. Comparing these methods, their relationships with the IS-2 derived h showed slight differences. However, the correlation between h and σ was stronger than h and S_{rms}. Therefore, using σ is potentially more reliable for training RCM data (e.g., model development) since it has a stronger correlation with h and is included in the ATL07 product. However, there were some areas that do not cover the σ of the ice, which encourages researchers to use the S_{rms} method and remove the errors. Thus, using both methods can give more reliable results (see Table 4.9.).

Table 4.9. The inter-relationships between IS-2 h, σ, and S_{rms} over FYI and MYI during winter.

	FYI			MYI		
	h & σ	h & S_{rms}	σ & S_{rms}	h & σ	h & S_{rms}	σ & S_{rms}
April 16th, 2020						
Correlation	0.83	0.78	0.80	0.68	0.62	0.65
R^2	60%	61%	65%	47%	38%	43%
April 22nd, 2020						
Correlation	0.86	0.71	0.65	0.76	0.68	0.56
R^2	75%	51%	43%	58%	47%	31%
April 7th, 2021						
Correlation	0.78	0.77	0.77	0.47	0.48	0.78
R^2	62%	60%	60%	23%	24%	61%

4.4.2. IS-2 properties and their relationships with RCM backscatter

RCM backscatter showed a stronger correlation with IS-2 ATL07 parameters during winter compared to melt onset and melt seasons (Table 4.4., Table 4.6., and Table 4.8.). The highest elevation shown in the along-track profiles of object-wise mean values of surface parameters (with an average elevation of 0.93 m) was related to the highest backscatter coefficients in that area. In contrast, the lowest elevation during winter is related to the FYI close to the edge of MYI or the FYI area between MYI and land.

Using RCM backscatter data in dB format, as anticipated, resulted in stronger correlation coefficients compared to power format. In this study, from C-band, RCM SAR images acquired during the winter season, HH, HV, and HH+HV backscatter are typically the most promising for estimating sea ice surface roughness and elevation (See Figures 4.14 and 4.15.). The relationship between elevation and backscatter are typically stronger than between roughness parameters and backscatter. Among these bands, HH+HV showed a higher potential for the estimation of FYI roughness. With a moderate incidence angle, HH+HV becomes more strongly correlated for FYI

roughness. The GLCM derived texture values were not explicitly addressed in this study due to weak overall relationships with IS-2 data.

Regarding incidence angle, HH and HH+HV from FYI, assessed from RCM data taken at low incidence angle, have stronger correlations with *h* compared to MYI. Whereas MYI *h* has stronger relationships with backscatter bands HH and HH+HV at high incidence angle, compared to FYI.

Regarding *h* and σ relationships (Figure 4.12.) and the relationships between highest backscatter and ice elevation (Figure 4.14.), HH+HV can best represent FYI using RCM image with low incidence angle during winter. HH+HV can represent MYI using high incidence angle during winter.

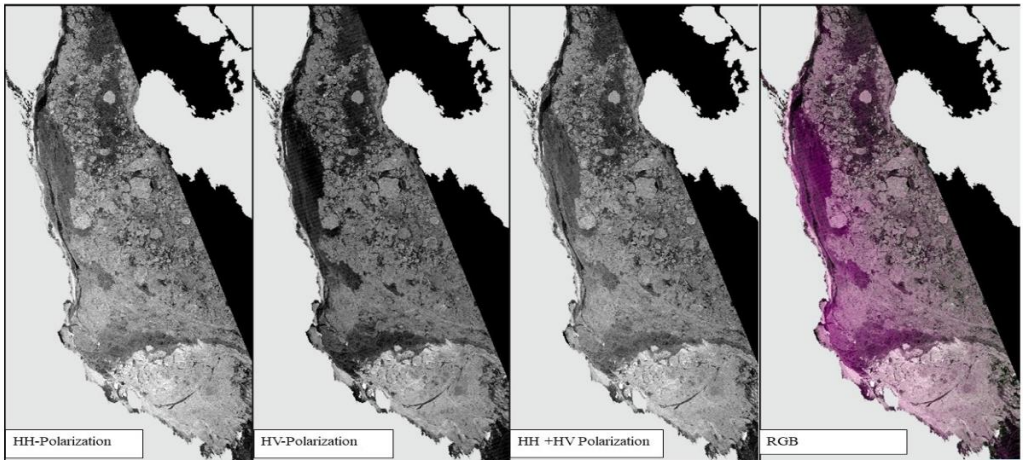

Figure 4.15.April 16th,2020, is an example to show the highest correlated bands with *h* and σ. All bands are shown in a decibel format. The RGB image is the combination of three bands.

Chapter Five: Thesis Summary and Future Recommendations

This thesis presents quantitative links between sea ice elevation and surface roughness, and C-band frequency SAR backscatter of FYI and MYI in the Canadian Arctic Archipelago in 2020 and 2021. This was achieved by using an object-based image analysis to link IS-2 laser altimeter derived sea ice elevation and surface roughness measurements, and spatially coincident RCM images providing backscatter. The results provided here provide a first-look at the potential for using C-band backscatter over wide swaths for ice surface elevation estimates during the winter period, based on comparisons to elevation data from IS-2 ATL07.

According to the correlation results, the following methods should be used to map the elevation of sea ice during the winter: (1) HH-polarization backscatter (r ~ 0.74) and a low incidence angle (FYI only), and (2) HH+HV polarization (r ~ 0.64) and low incidence angle (MYI only); (3) HH+HV polarization (r ~ 0.74) and high incidence angle (MYI only); and (4) HH-HV polarization (FYI) or HV (MYI) (r ~ 0.75 and 0.72, respectively) and moderate incidence angle. Therefore, HH+HV polarization is suggested here as the best representative band for FYI investigations employing RCM images with low incidence angle during winter, according to h and σ relationships (Figure 4.12.) and the correlations between backscatter and h (Figure 4.14.).

A natural surface roughness can be measured, but it is still difficult because point density and extent must be balanced. When surface roughness plays a key role in determining how strong sea ice is, the multiscale aspect of the elevation profile of the sea ice assumes increasing significance. Additionally, it demonstrates the thermodynamic responses of sea ice to stimuli, particularly in marginal, coastal, and seasonally ice-covered seas. The equipment and sensor limitations in this study and others could have an effect on the findings. This study is only

concerned with quantifying the relationships between RCM backscatter and IS-2 data over a landfast ice across three seasons in two years.

It is recommended to continue this research with a more in-depth study on the relationships between surface roughness and SAR backscatter during winter, as well as more studies on the relationship between IS-2 properties and RCM backscatter during melt-onset and melt seasons. In future studies considering less time difference between data collection is essential. Specifically, over the dynamic area, the time difference should be less than an hour.

References:

Ager, Thomas. 2013. “An Introduction to Synthetic Aperture Radar Imaging.” *Oceanography* 26 (2): 20–33. https://doi.org/10.5670/oceanog.2013.28.

AMSD. 2018. “Arctic Ice Regime Shipping System (AIRSS) Standard.” *Transport Canada*. https://tc.canada.ca/sites/default/files/migrated/tp12259e.pdf.

Arkett, Matthew, Dean Flett, Roger De Abreu, P. Clemete-Colon, John Woods, and Beaufort Sea. 2008. “EVALUATING ALOS-PALSAR FOR ICE MONITORING – WHAT CAN L-BAND DO FOR THE NORTH AMERICAN ICE SERVICE ? Canadian Ice Service – Meteorological Service of Canada - Environment Canada , Ottawa , National Ice Centre – Washington , D . C ., UNITED STATES.” *Analysis*, no. 1: 188–91.

Barber, D. G., and J. Iacozza. 2004. “Historical Analysis of Sea Ice Conditions in M’Clintock Channel and the Gulf of Boothia, Nunavut: Implications for Ringed Seal and Polar Bear Habitat.” *Arctic* 57 (1): 1–14. https://doi.org/10.14430/arctic478.

Barber, D. G., G. McCullough, D. Babb, A. S. Komarov, L. M. Candlish, J.V. Lukovich, M. Asplin, S. Prinsenberg, I. Dmitrenko, and S. Rysgaard. 2014. “Climate Change and Ice Hazards in the Beaufort Sea.” *Elementa: Science of the Anthropocene* 2 (1982): 000025. https://doi.org/10.12952/journal.elementa.000025.

Beckers, Justin F, Angelika H H Renner, Gunnar Spreen, Sebastian Gerland, and Christian Haas. 2015. “Sea-Ice Surface Roughness Estimates from Airborne Laser Scanner and Laser Altimeter Observations in Fram Strait and North of Svalbard” l (69): 235–44. https://doi.org/10.3189/2015AoG69A717.

Bertoia, Cheryl, Michael Manore, Henrik Steen Andersen, Chris O’Connors, Keld Q. Hansen, and Craig Evanego. 2004. “Synthetic Aperture Radar for Operational Ice Observation and Analysis at the U . S ., Canadian , and Danish National Ice Centers.” *Synthetic Aperture Radar Marine User’s Manual* 574 (574): 417–42.

Borsa, Adrian A., Helen Amanda Fricker, and Kelly M. Brunt. 2019. “A Terrestrial Validation of ICESat Elevation Measurements and Implications for Global Reanalyses.” *IEEE*

Transactions on Geoscience and Remote Sensing 57 (9): 6946–59. https://doi.org/10.1109/TGRS.2019.2909739.

Brekke, Camilla, Jakob Grahn, and Anthony P. Doulgeris. 2015. “Quad-Polarimetric SAR for Roughness and Deformation Characterization of Sea Ice at Hopen.” In *Proc. POLinSAR. 2015*, 729:26–30. http://adsabs.harvard.edu/abs/2015ESASP.729E..56B.

Cafarella, Silvie Marie, Randall Scharien, Torsten Geldsetzer, Stephen Howell, Christian Haas, Rebecca Segal, and Sasha Nasonova. 2019. “Estimation of Level and Deformed First-Year Sea Ice Surface Roughness in the Canadian Arctic Archipelago from C- and L-Band Synthetic Aperture Radar.” *Canadian Journal of Remote Sensing* 45 (3–4): 457–75. https://doi.org/10.1080/07038992.2019.1647102.

Carlström, A, and L M H Ulander. 1995. “Validation of Backscatter Models for Level and Deformed Sea-Ice in ERS-l SAR Images.” *Int. J.Remote Sens* 16: 3245–3266. https://doi.org/10.1080/01431169508954629.

Casey, J. Alec, Stephen E.L. Howell, Adrienne Tivy, and Christian Haas. 2016. “Separability of Sea Ice Types from Wide Swath C- and L-Band Synthetic Aperture Radar Imagery Acquired during the Melt Season.” *Remote Sensing of Environment* 174: 314–28. https://doi.org/10.1016/j.rse.2015.12.021.

Casey J. Alexander. 2018. “Evaluating Recent Advances in Active Microwave Remote Sensing for Arctic Sea Ice Monitoring.” University of Alberta. https://era.library.ualberta.ca/items/94872987-6230-4434-8412-4f191a98ee63.

Castellani, G., C. Lüpkes, S. Hendricks, and R. Gerdes. 2014. “Variability of Arctic Sea-Ice Topography and Its Impact on the Atmospheric Surface Drag.” *Journal of Geophysical Research: Oceans* 119 (10): 6743–62. https://doi.org/10.1002/2013JC009712.

Chelton, Dudley B., and Frank J. Wentz. 1986. “Further Development of an Improved Altimeter Wind Speed Algorithm.” *Journal of Geophysical Research* 91 (C12): 14250. https://doi.org/10.1029/jc091ic12p14250.

Chudley, Thomas R., Poul Christoffersen, Samuel H. Doyle, Antonio Abellan, and Neal Snooke.

2019. “High-Accuracy UAV Photogrammetry of Ice Sheet Dynamics with No Ground Control.” *Cryosphere* 13 (3): 955–68. https://doi.org/10.5194/tc-13-955-2019.

Comiso, Josefino C., and Dorothy K. Hall. 2014. “Climate Trends in the Arctic as Observed from Space.” *Wiley Interdisciplinary Reviews: Climate Change* 5 (3): 389–409. https://doi.org/10.1002/wcc.277.

Curry, Judith A., Julie L. Schramm, and Elizabeth E. Ebert. 1995. “Sea Ice-Albedo Climate Feedback Mechanism.” *Journal of Climate* 8 (2): 240–47. https://doi.org/10.1175/1520-0442(1995)008<0240:SIACFM>2.0.CO;2.

Dabboor, M., B. Montpetit, and S. Howell. 2018. “Assessment of the High Resolution SAR Mode of the RADARSAT Constellation Mission for First Year Ice and Multiyear Ice Characterization.” *Remote Sensing* 10 (4): 594. https://doi.org/10.3390/rs10040594.

Dammann, Dyre Oliver, Hajo Eicken, Andrew R Mahoney, Eyal Saiet, Franz J Meyer, and John C. Craig George. 2018. “Traversing Sea Ice-Linking Surface Roughness and Ice Trafficability Through SAR Polarimetry and Interferometry.” *IEEE Journal of Selected Topics in Applied Earth Observations and Remote Sensing* 11 (2): 416–33. https://doi.org/10.1109/JSTARS.2017.2764961.

Déry, Stephen J., and Peter A. Taylor. 1996. “Some Aspects of the Interaction of Blowing Snow with the Atmospheric Boundary Layer.” *Hydrological Processes* 10 (10): 1345–58. https://doi.org/10.1002/(SICI)1099-1085(199610)10:10<1345::AID-HYP465>3.0.CO;2-2.

Dierking. 2010a. “Mapping of Different Sea Ice Regimes Using Images from Sentinel-1 and ALOS Synthetic Aperture Radar.” *IEEE Transactions on Geoscience and Remote Sensing* 48 (3 PART 1): 1045–58. https://doi.org/10.1109/TGRS.2009.2031806.

———. 2010b. “Mapping of Different Sea Ice Regimes Using Images From Sentinel-1 and ALOS Synthetic Aperture Radar.” *IEEE Transactions on Geoscience and Remote Sensing* 48 (3): 1045–58. https://doi.org/10.1109/TGRS.2009.2031806.

Dierking, and Busche. 2006. “Sea Ice Monitoring by L-Band SAR : An Assessment Based on Literature and Comparisons Of.” *East* 44 (2): 957–70.

Dierking, W. 1995. “Laser Profiling of the Ice Surface Topography during the Winter Weddel Gyre Study 1992.” *Journal of Geophysical Research* 100 (C3): 4807–20. https://doi.org/10.1029/94JC01938.

Dierking, W. 1999. “Multifrequency Scatterometer Measurements of Baltic Sea Ice during EMAC-95.” *International Journal of Remote Sensing* 20 (2): 349–72. https://doi.org/10.1080/014311699213488.

Dierking, Wolfgang. 2013. “Sea Ice Monitoring by Synthetic Aperture Radar.” *Oceanography* 26 (2): 100–111. https://doi.org/10.5670/oceanog.2013.33.

Dierking, Wolfgang, and Jørgen Dall. 2008. “Sea Ice Deformation State from Synthetic Aperture Radar Imagery - Part II: Effects of Spatial Resolution and Noise Level.” *IEEE Transactions on Geoscience and Remote Sensing* 46 (8): 2197–2207. https://doi.org/10.1109/TGRS.2008.917267.

Doble, Martin J., Henriette Skourup, Peter Wadhams, and Cathleen A. Geiger. 2011. “The Relation between Arctic Sea Ice Surface Elevation and Draft: A Case Study Using Coincident AUV Sonar and Airborne Scanning Laser.” *Journal of Geophysical Research: Oceans* 116 (11): 1–12. https://doi.org/10.1029/2011JC007076.

Drinkwater, Mark R., Richard Francis, Guy Ratier, and Duncan J. Wingham. 2004. “The European Space Agency’s Earth Explorer Mission CryoSat: Measuring Variability in the Cryosphere.” *Annals of Glaciology* 39: 313–20. https://doi.org/10.3189/172756404781814663.

Drucker, Robert. 2003. “Observations of Ice Thickness and Frazil Ice in the St. Lawrence Island Polynya from Satellite Imagery, Upward Looking Sonar, and Salinity/Temperature Moorings.” *Journal of Geophysical Research* 108 (C5): 1–18. https://doi.org/10.1029/2001jc001213.

Duncan, K, and S. L. Farrell. 2022. “Determining Variability in Arctic Sea Ice Pressure Ridge Topography With ICESat-2.” *Geophysical Research Letters* 49 (18): 1–10. https://doi.org/10.1029/2022GL100272.

Dyne, Michele M. Van, Costas Tsatsoulis, and Florence Fetterer. 1998. “Analyzing Lead Information from SAR Images.” *IEEE Transactions on Geoscience and Remote Sensing* 36 (2): 647–60. https://doi.org/10.1109/36.662745.

Eicken, Hajo, and Andrew R. Mahoney. 2014. “Sea Ice: Hazards, Risks, and Implications for Disasters.” *Coastal and Marine Hazards, Risks, and Disasters*, no. March 2016: 381–401. https://doi.org/10.1016/B978-0-12-396483-0.00013-3.

Eicken, Hajo, and Andrew R Mahoney. 2015. *Sea Ice : Hazards , Risks , and Implications for Disasters*. *Coastal and Marine Hazards, Risks, and Disasters*. Elsevier Inc. https://doi.org/10.1016/B978-0-12-396483-0.00013-3.

Eriksson, Leif E.B., Karin Borenäs, Wolfgang Dierking, Anders Berg, Maurizio Santoro, Per Pemberton, Henrik Lindh, and Bengt Karlson. 2010. “Evaluation of New Spaceborne SAR Sensors for Sea-Ice Monitoring in the Baltic Sea.” *Canadian Journal of Remote Sensing* 36 (sup1): S56–73. https://doi.org/10.5589/m10-020.

Facility, Alaska S A R, Standard Beam Sar, S A R Faq, Mcmurdo Station, Through Asf, The Radarsat-, Antarctic Mapping Mission, et al. 1996. “RADARSAT-1 Standard Beam SAR Images Summary:” *Delta*, no. November 1995.

Farrell, S. L., K. Duncan, E. M. Buckley, J. Richter-Menge, and R. Li. 2020. “Mapping Sea Ice Surface Topography in High Fidelity With ICESat-2.” *Geophysical Research Letters* 47 (21). https://doi.org/10.1029/2020GL090708.

Fassnacht, S. R., M. W. Williams, and M. V. Corrao. 2009. “Changes in the Surface Roughness of Snow from Millimetre to Metre Scales.” *Ecological Complexity* 6 (3): 221–29. https://doi.org/10.1016/j.ecocom.2009.05.003.

Feltham, Daniel L. 2008. “Sea Ice Rheology.” https://doi.org/10.1146/annurev.fluid.40.111406.102151.

Fetterer, F., M Savoie, S. Helfrich, and P. Clemente-Colon. 2010. “Multisensor Analyzed Sea Ice Extent - Northern Hemisphere (MASIE-NH), Version 1. Bering Sea Ice Extent 2007-2020.”

Fissel, D B, J R Marko, and H Melling. 2015. “Advances in Upward Looking Sonar Technology

for Studying the Processes of Change in Arctic Ocean Ice Climate" 8778: 8–18. https://doi.org/10.1080/1755876X.2008.11081884.

Fors, Ane S, Camilla Brekke, Sebastian Gerland, Anthony P Doulgeris, and Justin F Beckers. 2016. "Late Summer Arctic Sea Ice Surface Roughness Signatures in C-Band SAR Data." *IEEE Journal of Selected Topics in Applied Earth Observations and Remote Sensing* 9 (3): 1199–1215. https://doi.org/10.1109/JSTARS.2015.2504384.

Francis, C.R. 2007. "CryoSat Mission and Data Description." *European Space Agency Report CS-RP-ESA-SY-0059*, 2007.

Francis, Oceana P., and David E. Atkinson. 2012. "Synoptic Forcing of Wave States in the Southeast Chukchi Sea, Alaska, at Nearshore Locations." *Natural Hazards* 62 (3): 1273–1300. https://doi.org/10.1007/s11069-012-0148-y.

Fujisaki-manome, Ayumi, and Hajime Yamaguchi. 2009. "Measurements of Air-Ice Drag Coefficient over the Ice-Covered Sea of Okhotsk Measurements of Air-Ice Drag Coefficient over the Ice- Covered Sea of Okhotsk," no. August. https://doi.org/10.1007/s10872-009-0042-8.

Fukamachi, Yasushi, Daisuke Simizu, Kay I. Ohshima, Hajo Eicken, Andrew R. Mahoney, Katsushi Iwamoto, Erika Moriya, and Sohey Nihashi. 2017. "Sea-Ice Thickness in the Coastal Northeastern Chukchi Sea from Moored Ice-Profiling Sonar." *Journal of Glaciology* 63 (241): 888–98. https://doi.org/10.1017/jog.2017.56.

Gegiuc, Alexandru, Markku Similä, Juha Karvonen, Mikko Lensu, Marko Mäkynen, and Jouni Vainio. 2018. "Estimation of Degree of Sea Ice Ridging Based on Dual-Polarized C-Band SAR Data," 343–64.

Geldsetzer, Torsten, Matt Arkett, Tom Zagon, François Charbonneau, John J. Yackel, and Randall K. Scharien. 2015. "All-Season Compact-Polarimetry C-Band SAR Observations of Sea Ice." *Canadian Journal of Remote Sensing* 41 (5): 485–504. https://doi.org/10.1080/07038992.2015.1120661.

Geldsetzer, Torsten, and John J. Yackel. 2009. "Sea Ice Type and Open Water Discrimination

Using Dual Co-Polarized C-Band SAR" 35 (1): 73–84. https://doi.org/10.5589/m08-075.

Gill, Jagvijay P.S., and John J. Yackel. 2012. "Evaluation of C-Band SAR Polarimetric Parameters for Discrimination of First-Year Sea Ice Types." *Canadian Journal of Remote Sensing* 38 (3): 306–23. https://doi.org/10.5589/m12-025.

Gill, Jagvijay P.S., John J. Yackel, and Torsten Geldsetzer. 2013. "Analysis of Consistency in First-Year Sea Ice Classification Potential of C-Band SAR Polarimetric Parameters." *Canadian Journal of Remote Sensing* 39 (2): 101–17. https://doi.org/10.5589/m13-016.

Goff, J. A., W. K. Stewart, H. Singh, and Xiaoou Tang. 1995. "Quantitative Analysis of Sea Ice Draft 2. Application of Stochastic Modeling to Intersecting Topographic Profiles." *Journal of Geophysical Research* 100 (C4): 7005–17. https://doi.org/10.1029/94JC03201.

Gupta, M., D. G. Barber, R. K. Scharien, and D. Isleifson. 2012. "Detection and Classification of Surface Roughness in an Arctic Marginal Sea Ice Zone." *Hydrological Processes* 28 (3): 599–609. https://doi.org/10.1002/hyp.9593.

Gupta, Mukesh, Randall K. Scharien, David G. Barber, Dmitrii Murashkin, Gunnar Spreen, Marcus Huntemann, Wolfgang Dierking, et al. 2019. "Potential of RADARSAT-2 Data for Operational Sea Ice Monitoring." *Canadian Journal of Remote Sensing* 30 (3): 448–61. https://doi.org/10.5589/m04-011.

Haas, Christian. 2010. "Dynamics Versus Thermodynamics: The Sea Ice Thickness Distribution." *Sea Ice: Second Edition,* 113–51. https://doi.org/10.1002/9781444317145.ch4.

Haas, Christian, and Stephen E L Howell. 2015. "Ice Thickness in the Northwest Passage," 1–8. https://doi.org/10.1002/2015GL065704.Received.

Haas, Christian, John Lobach, Stefan Hendricks, Lasse Rabenstein, and Andreas Pfaf. 2009. "Helicopter-Borne Measurements of Sea Ice Thickness , Using a Small and Lightweight , Digital EM System" 67: 234–41. https://doi.org/10.1016/j.jappgeo.2008.05.005.

Haas, Liu, and Martin. 1999. "Retrieval of Antarctic Sea-Ice Pressure Ridge Frequencies from ERS SAR Imagery by Means of in Situ Laser Profiling and Usage of a Neural Network."

International Journal of Remote Sensing 20 (15–16): 3111–23. https://doi.org/10.1080/014311699211642.

Hall-Beyer, Mryka. 2017. "Glcm Texture: A Tutorial," no. February. https://doi.org/10.13140/RG.2.2.12424.21767.

Harding, D.J., P. Dabney, A.W. Yu, S.R. Valett, and E. Timmons. 2015. "SIMPL Measurements of Laser Light Penetration into Snow, Ice and Water: The 2015 Greenland Airborne Campaign in Support of ICESat-2." In *AGU Fall Meeting Abstracts*, 2015:C41C-0708.

Haverkamp, Donna, Leen Kiat Soh, and Costas Tsatsoulis. 1995. "A Comprehensive, Automated Approach to Determining Sea Ice Thickness from SAR Data." *IEEE Transactions on Geoscience and Remote Sensing* 33 (1): 46–57. https://doi.org/10.1109/36.368223.

Heinrichs, John F., Donald J. Cavalieri, and Thorsten Markus. 2006. "Assessment of the AMSR-E Sea Ice Concentration Product at the Ice Edge Using RADARS AT-1 and MODIS Imagery." *IEEE Transactions on Geoscience and Remote Sensing* 44 (11): 3070–79. https://doi.org/10.1109/TGRS.2006.880622.

Hibler, W D. 1972. "Removal of Aircraft Altitude Variation from Segments between the Identified Is to Be Expected . All the Minimum Points" 77 (36).

Hoffman, Regis, and Eric Krotkov. 1989. "Terrain Roughness Measurement from Elevation Maps." *Mobile Robots IV* 1195: 104. https://doi.org/10.1117/12.969874.

Hong, Sungwook. 2010. "Remote Sensing of Environment Detection of Small-Scale Roughness and Refractive Index of Sea Ice in Passive Satellite Microwave Remote Sensing." *Remote Sensing of Environment* 114 (5): 1136–40. https://doi.org/10.1016/j.rse.2009.12.015.

Hopkins, Mark A. 1998. "Four Stages of Pressure Ridging." *Journal of Geophysical Research: Oceans* 103 (C10): 21883–91. https://doi.org/10.1029/98JC01257.

Hutter, Nils, Lorenzo Zampieri, and Martin Losch. 2019. "Leads and Ridges in Arctic Sea Ice from RGPS Data and a New Tracking Algorithm." *Cryosphere* 13 (2): 627–45. https://doi.org/10.5194/tc-13-627-2019.

Inggs, M R, and R T Lord. 2005. “Current Applications of Imaging Radar.” *Int. Conf. on Advanced Remote Sensing for Earth Observation Systems, Techniques and Applications* XXXVI-1/w1 (January).

Jensen, John R. 2000. *Remote Sensing of the Environment: An Earth Resource Perspective*. Edited by Saddle River. Prentice-Hall, Inc.

Johansson, A. M., J. A. King, A. P. Doulgeris, S. Gerland, S. Singha, G. Spreen, and T. Busche. 2017. “Combined Observations of Arctic Sea Ice with Near-Coincident Colocated X-Band, C-Band, and L-Band SAR Satellite Remote Sensing and Helicopter-Borne Measurements.” *Journal of Geophysical Research: Oceans* 122 (1): 669–91. https://doi.org/10.1002/2016JC012273.

Key, J., and A. S. McLaren. 1991. “Fractal Nature of the Sea Ice Draft Profile.” *Geophysical Research Letters* 18 (8): 1437–40. https://doi.org/10.1029/91GL01761.

Kim, Jin-Woo, Duk-jin Kim, and Byong Jun Hwang. 2012. “Characterization of Arctic Sea Ice Thickness Using High-Resolution Spaceborne Polarimetric SAR Data.” *IEEE Transactions on Geoscience and Remote Sensing* 50 (1): 13–22. https://doi.org/10.1109/TGRS.2011.2160070.

Kim, Jong Min, Byung Ju Sohn, Sang Moo Lee, Rasmus Tage Tonboe, Eui Jong Kang, and Hyun Cheol Kim. 2020. “Differences Between ICESat and CryoSat-2 Sea Ice Thicknesses Over the Arctic: Consequences for Analyzing the Ice Volume Trend.” *Journal of Geophysical Research: Atmospheres* 125 (22). https://doi.org/10.1029/2020JD033103.

Koo, Young Hyun, Ruibo Lei, Yubing Cheng, Bin Cheng, Hongjie Xie, Mario Hoppmann, Nathan T. Kurtz, Stephen F. Ackley, and Alberto M. Mestas-Nuñez. 2021. “Estimation of Thermodynamic and Dynamic Contributions to Sea Ice Growth in the Central Arctic Using ICESat-2 and MOSAiC SIMBA Buoy Data.” *Remote Sensing of Environment* 267 (July). https://doi.org/10.1016/j.rse.2021.112730.

Kwok, Markus, Kurtz, Petty, Neumann, Farrell, Cunningham, Hancock, Ivanoff, and Wimert. 2019. “Surface Height and Sea Ice Freeboard of the Arctic Ocean From ICESat-2: Characteristics and Early Results.” *Journal of Geophysical Research: Oceans* 124 (10):

6942–59. https://doi.org/10.1029/2019JC015486.

Kwok, R. 2001. “Deformation of the Arctic Ocean Sea Ice Cover between November 1996 and April 1997: A Qualitative Survey,” no. April: 315–22. https://doi.org/10.1007/978-94-015-9735-7_26.

———. 2010. “Satellite Remote Sensing of Sea-Ice Thickness and Kinematics: A Review.” *Journal of Glaciology* 56 (200): 1129–40. https://doi.org/10.3189/002214311796406167.

———. 2014. “Declassified High-Resolution Visible Imagery for Arctic Sea Ice Investigations: An Overview.” *Remote Sensing of Environment* 142: 44–56. https://doi.org/10.1016/j.rse.2013.11.015.

Kwok, R., G. F. Cunningham, M. Wensnahan, I. Rigor, H. J. Zwally, and D. Yi. 2009. “Thinning and Volume Loss of the Arctic Ocean Sea Ice Cover: 2003-2008.” *Journal of Geophysical Research: Oceans* 114 (7): 2003–8. https://doi.org/10.1029/2009JC005312.

Kwok, R, S V Ngh, S H Yueh, and D D Huynh. 1995. “Retrieval of Thin Ice Thickness from Multifrequency Polarimetric SAR Data - KWOK ET AL. 1995.Pdf” 374 (June 1994): 361–74.

Laine, Vesa, Terhikki Manninen, Aku Riihelä, and Kaj Andersson. 2011. “Shortwave Broadband Black-Sky Surface Albedo Estimation for Arctic Sea Ice Using Passive Microwave Radiometer Data.” *Journal of Geophysical Research Atmospheres* 116 (16): 1–16. https://doi.org/10.1029/2011JD015700.

Lang, Wenhui, Pan Zhang, Jie Wu, Yang Shen, and Xuezhi Yang. 2016. “Incidence Angle Correction of SAR Sea Ice Data Based on Locally Linear Mapping.” *IEEE Transactions on Geoscience and Remote Sensing* 54 (6): 3188–99. https://doi.org/10.1109/TGRS.2015.2513159.

Laxon S., Walsh J. E., Wadhams P., Johannessen O. M., and Miles M. 2004. “Sea-Ice Observations.” In *Mass Balance of the Cryosphere*, edited by John Houghton, 337–366. Cambridg university.

Laxon, Seymour W., Katharine A. Giles, Andy L. Ridout, Duncan J. Wingham, Rosemary

Willatt, Robert Cullen, Ron Kwok, et al. 2013. “CryoSat-2 Estimates of Arctic Sea Ice Thickness and Volume.” *Geophysical Research Letters* 40 (4): 732–37. https://doi.org/10.1002/grl.50193.

Lee, J.S. 1986. “Speckle Analysis and Smoothing of Synthetic Aperture Radar Images” 17: 24–32.

Lei, Ruibo, Xiangshan Tian-Kunze, Matti Leppäranta, Jia Wang, Lars Kaleschke, and Zhanhai Zhang. 2016. “Changes in Summer Sea Ice, Albedo, and Portioning of Surface Solar Radiation in the Pacific Sector of Arctic Ocean during 1982-2009.” *Journal of Geophysical Research: Oceans* 121 (8): 5470–86. https://doi.org/10.1002/2016JC011831.

Leppäranta, Matti. 2005. *The Drift of Sea Ice*. 2nd ed. New York, USA: Springer-Verlag, Heidelberg. https://doi.org/10.1007/978-3-642-04683-4.

Lisle, Daniel De, and Steve Iris. 2018. “RADARSAT Constellation Mission Status Update.” *Proceedings of the European Conference on Synthetic Aperture Radar, EUSAR*, 1–5.

Livingstone, C.E., and M.R. Drinkwater. 1991. “Springtime C-Band SAR Backscatter Signatures of Labrador Sea Marginal Ice: Measurements versus Modeling Predictions.” *IEEE Transactions on Geoscience and Remote Sensing* 29 (1): 29–41. https://doi.org/10.1109/36.103290.

Lüpkes, Christof, Vladimir M. Gryanik, Jörg Hartmann, and Edgar L. Andreas. 2012. “A Parametrization, Based on Sea Ice Morphology, of the Neutral Atmospheric Drag Coefficients for Weather Prediction and Climate Models.” *Journal of Geophysical Research Atmospheres* 117 (13): 1–18. https://doi.org/10.1029/2012JD017630.

Mäkynen, M, and M Hallikainen. 2002. “INVESTIGATION ON THE INCIDENCE ANGLE DEPENDENCE OF THE MEAN C-BAND HH-POLARIZATION BACKSCATTERING SIGNATURES OF THE BALTIC SEA ICE.” *IEEE Trans. Geosci. Remote Sens* 40: 2593–2605.

Mäkynen, Marko P., A. Terhikki Manninen, Markku H. Similä, Juha A. Karvonen, and Martti T. Hallikainen. 2002. “Incidence Angle Dependence of the Statistical Properties of C-Band

HH-Polarization Backscattering Signatures of the Baltic Sea Ice." *IEEE Transactions on Geoscience and Remote Sensing* 40 (12): 2593–2605. https://doi.org/10.1109/TGRS.2002.806991.

Maxwell, J.B. 1981. "Climatic Regions of the Canadian Arctic Islands." *Arctic* 34 (3): 225–40. https://doi.org/10.14430/arctic2525.

Maykut, Gary A., and Norbert Untersteiner. 1971. "Some Results from a Time-Dependent Thermodynamic Model of Sea Ice." *Journal of Geophysical Research* 76 (6): 1550–75. https://doi.org/10.1029/JC076i006p01550.

McCandless Jr. W. (Walt) Samuel, and Christopher R. Jackson. 2004. "SAR Measurements of Sea Ice." In *Synthetic Aperture Radar Marine User's Manual*. Washington, D.C.: National Oceanic and Atmospheric Administration.

Meier, Walter N. 2005. "Comparison of Passive Microwave Ice Concentration Algorithm Retrievals with AVHRR Imagery in Arctic Peripheral Seas." *IEEE Transactions on Geoscience and Remote Sensing* 43 (6): 1324–37. https://doi.org/10.1109/TGRS.2005.846151.

Melling, H. 1998. "Detection of Features in First-Year Pack Ice by Synthetic Aperture Radar (SAR)." *International Journal of Remote Sensing* 19 (6): 1223–49. https://doi.org/10.1080/014311698215702.

Melling, Humfrey. 2002. "Sea Ice of the Northern Canadian Arctic Archipelago." *Journal of Geophysical Research: Oceans* 107 (11). https://doi.org/10.1029/2001jc001102.

Micheletti, Natan, Jim H Chandler, and Stuart N Lane. 2015. "Structure-from-Motion Photogrammetry." In *Geomorphological Techniques (Online Edition).*, edited by L.E. Clarke and J.M. (Eds.) Nield, 31:36–39. British Society for Geomorphology. https://repository.lboro.ac.uk/articles/journal_contribution/Structure_from_motion_SFM_photogrammetry/9457355.

Mladenova, Iliana E., Thomas J. Jackson, Rajat Bindlish, and Scott Hensley. 2013. "Incidence Angle Normalization of Radar Backscatter Data." *IEEE Transactions on Geoscience and*

Remote Sensing 51 (3): 1791–1804. https://doi.org/10.1109/TGRS.2012.2205264.

Moen, M. A.N., A. P. Doulgeris, S. N. Anfinsen, A. H.H. Renner, N. Hughes, S. Gerland, and T. Eltoft. 2013. "Comparison of Feature Based Segmentation of Full Polarimetric SAR Satellite Sea Ice Images with Manually Drawn Ice Charts." *Cryosphere* 7 (6): 1693–1705. https://doi.org/10.5194/tc-7-1693-2013.

Moen, Mari-ann, Anthony Paul Doulgeris, Stian Normann Anfinsen, and Angelika H H Renner. 2013. "Sea Ice Images with Manually Drawn Ice Charts The Cryosphere Comparison of Feature Based Segmentation of Full Polarimetric SAR Satellite Sea Ice Images with Manually Drawn Ice Charts," no. November. https://doi.org/10.5194/tc-7-1693-2013.

Mohammadi-Aragh, M., H. F. Goessling, M. Losch, N. Hutter, and T. Jung. 2018. "Predictability of Arctic Sea Ice on Weather Time Scales." *Scientific Reports* 8 (1): 1–7. https://doi.org/10.1038/s41598-018-24660-0.

Moreira, A, P Prats-Iraola, M Younis, G Krieger, I Hajnsek, and K P Papathanassiou. 2013. "A Tutorial on Synthetic Aperture Radar." *Geoscience and Remote Sensing Magazine, IEEE* 1 (1): 6–43. https://doi.org/10.1109/MGRS.2013.2248301.

Morey, R. M., A. Kovacs, and G. F.N. Cox. 1984. "Electromagnetic Properties of Sea Ice." *Cold Regions Science and Technology* 9 (1): 53–75. https://doi.org/10.1016/0165-232X(84)90048-X.

MSC. 2005. *MANICE: Manual of Standard Procedures for Observing and Reporting Ice Conditions*. *Meteorological Service of Canada Catalogue*. Revised Ni. http://publications.gc.ca/collections/collection_2013/ec/En56-175-2005-eng.pdf.

Murashkin, Dmitrii, Gunnar Spreen, Marcus Huntemann, and Wolfgang Dierking. 2018. "Method for Detection of Leads from Sentinel-1 SAR Images." *Annals of Glaciology* 59 (76pt2): 124–36. https://doi.org/10.1017/aog.2018.6.

Nakamura, Kazuki, Hiroyuki Wakabayashi, Kazuhiro Naoki, and Fumihiko Nishio. 2005. "Observation of Sea-Ice Thickness in the Sea of Okhotsk by Using Dual-Frequency and Fully." *East* 43 (11): 2460–69.

National Snow and Ice Data Center. 2009. “Laser Operational Periods : ICESat / GLAS Data.” https://nsidc.org/sites/nsidc.org/files/technical-references/LaserOperationalPeriods.pdf.

———. 2019. “Arctic Sea Ice Reaches Second Lowest Minimum in Satellite Record | Arctic Sea Ice News and Analysis.” *NSIDC*. http://nsidc.org/arcticseaicenews/2019/09/.

Neumann, Thomas A., Anthony J. Martino, Thorsten Markus, Sungkoo Bae, Megan R. Bock, Anita C. Brenner, Kelly M. Brunt, et al. 2019. “The Ice, Cloud, and Land Elevation Satellite – 2 Mission: A Global Geolocated Photon Product Derived from the Aadvanced Ttopographic Llaser Aaltimeter Ssystem.” *Remote Sensing of Environment* 233 (September): 111325. https://doi.org/10.1016/j.rse.2019.111325.

Nghiem, S. V., and C. Bertoia. 2001. “Study of Multi-Polarization c-Band Backscatter Signatures for Arctic Sea Ice Mapping with Future Satellite SAR.” *Canadian Journal of Remote Sensing* 27 (5): 387–402. https://doi.org/10.1080/07038992.2001.10854882.

Oh, Yisok, Kamal Sarabandi, and Fawwaz T. Ulaby. 1992. “An Empirical Model and an Inversion Technique for Radar Scattering from Bare Soil Surfaces.” *IEEE Transactions on Geoscience and Remote Sensing* 30 (2): 370–81. https://doi.org/10.1109/36.134086.

Onstott, Robert G. 1992. “SAR and Scatterometer Signatures of Sea Ice.” In *In Microwave Remote Sensing of Sea Ice*, edited by F. Carsey, 68:73–104. Washington, DC, USA: AGU. https://doi.org/10.1029/gm068p0073.

Perovich., W. Meier, M. Tschudi, S. Farrell, S. Hendricks, S. Gerland, L. Kaleschke, et al. 2019. “Arctic Report Card 2019 Arctic Ecosystems and Communities Are Increasingly at Risk,” no. December: 88–94. https://arctic.noaa.gov/Report-Card/Report-Card-2019/ArtMID/7916/ArticleID/841/Sea-Ice.

Perovich, Donald K., and Christopher Polashenski. 2012. “Albedo Evolution of Seasonal Arctic Sea Ice.” *Geophysical Research Letters* 39 (8): 1–6. https://doi.org/10.1029/2012GL051432.

Peterson, I K, S J Prinsenberg, and J S Holladay. 2008. “Observations of Sea Ice Thickness , Surface Roughness and Ice Motion in Amundsen Gulf” 113 (February): 1–14.

https://doi.org/10.1029/2007JC004456.

Petty, A. A., N. T. Kurtz, R. Kwok, T. Markus, and T. A. Neumann. 2020. “Winter Arctic Sea Ice Thickness From ICESat-2 Freeboards.” *Journal of Geophysical Research: Oceans* 125 (5): 1–28. https://doi.org/10.1029/2019JC015764.

Petty, A. A., M. C. Tsamados, N. T. Kurtz, S. L. Farrell, T. Newman, J. P. Harbeck, D. L. Feltham, and J. A. Richter-Menge. 2016. “Characterizing Arctic Sea Ice Topography Using High-Resolution IceBridge Data.” *The Cryosphere Discussions* 9 (6): 6495–6543. https://doi.org/10.5194/tcd-9-6495-2015.

Petty, Alek A., and Ron Kwok. 2020. “ATL07/10 - Notes to Users and Known Issues,” 10. https://nsidc.org/sites/nsidc.org/files/technical-references/ICESat2_ATL07_ATL10_Known_Issues_v003_Sept2020.pdf.

Pitas, I., and A. N. Venetsanopoulos. 1993. “Application of Adaptive Order Statistic Filters in Digital Image/Image Sequence Filtering.” *Proceedings - IEEE International Symposium on Circuits and Systems* 1 (4): 327–30. https://doi.org/10.1109/iscas.1993.692647.

Pizzolato, Larissa, Stephen E.L. Howell, Chris Derksen, Jackie Dawson, and Luke Copland. 2014. “Changing Sea Ice Conditions and Marine Transportation Activity in Canadian Arctic Waters between 1990 and 2012.” *Climatic Change* 123 (2): 161–73. https://doi.org/10.1007/s10584-013-1038-3.

Raju, Rajeswari, Tomas Maul, and Andrzej Bargiela. 2015. “New Image Processing Pipelines for Membrane Detection.” *Journal of the Institute of Industrial Applications Engineers* 3 (1): 15–23. https://doi.org/10.12792/jiiae.3.15.

Ramsay, B., T. Hirose, M. Manore, J. Falkingham, R. Gale, D. Barber, M. Shokr, B. Danielowicz, B. Gorman, and C. Livingstone. 1993. “Potential of Radarsat for Sea Ice Applications.” *Canadian Journal of Remote Sensing* 19 (4): 352–62. https://doi.org/10.1080/07038992.1993.10874570.

Remund, Quinn P., and David G. Long. 1999. “Sea Ice Extent Mapping Using Ku Band Scatterometer Data.” *Journal of Geophysical Research: Oceans* 104 (C5): 11515–27.

https://doi.org/10.1029/98jc02373.

Remy, F., B. Legresy, and P. Vincent. 1999. “New Scientific Opportunities from Ka-Band Altimetry.” *International Geoscience and Remote Sensing Symposium (IGARSS)* 1 (33): 506–8. https://doi.org/10.1109/igarss.1999.773548.

Rémy, Frédérique, and Soazig Parouty. 2009. “Antarctic Ice Sheet and Radar Altimetry: A Review.” *Remote Sensing* 1 (4): 1212–39. https://doi.org/10.3390/rs1041212.

Richards, John A. 2009. *Remote Sensing with Imaging Radar*. Verlag Berlin Heidelberg: Springer. https://doi.org/10.1007/978-3-642-02020-9_10.

Rothrock, D. A., and A. S. Thorndike. 1980. “Geometric Properties of the Underside of Sea Ice.” *Journal of Geophysical Research* 85 (C7): 3955–63. https://doi.org/10.1029/JC085iC07p03955.

Sachs, Lothar. 1992. *Angewandte Statistik*. *Angewandte Statistik*. Berlin, Heidelberg: Springer Berlin Heidelberg. https://doi.org/10.1007/978-3-662-05747-6.

Saldern, Carola Von, Thomas Busche, Christian Haas, and Wolfgang Dierking. 2005. “Analysis of Sea Ice Surface Roughness and Thickness Profiles for Improvement of SAR Ice Type Classification.” *European Space Agency, (Special Publication) ESA SP*, no. 572: 2159–64.

Scharien, Randall Kenneth, and Sasha Nasonova. 2020. “Incidence Angle Dependence of Texture Statistics From Sentinel-1 HH-Polarization Images of Winter Arctic Sea Ice.” *IEEE Geoscience and Remote Sensing Letters*, 5–9. https://doi.org/10.1109/LGRS.2020.3039739.

Scheuchl, Bernd, Ian Cumming, and Irena Hajnsek. 2005. “Classification of Fully Polarimetric Single- and Dual-Frequency SAR Data of Sea Ice Using the Wishart Statistics.” *Canadian Journal of Remote Sensing* 31 (1): 61–72. https://doi.org/10.5589/m04-060.

Scheuchl, Bernd, Dean Flett, Ron Caves, and Ian Cumming. 2004. “Potential of RADARSAT-2 Data for Operational Sea Ice Monitoring.” *Canadian Journal of Remote Sensing* 30 (3): 448–61. https://doi.org/10.5589/m04-011.

Schulson, Erland M., and Paul Duval. 2009. *Creep and Fracture of Ice*. Vol. 57. Cambridge:

Cambridge University Press. https://doi.org/10.1017/CBO9780511581397.

Segal, Rebecca A., Randall K. Scharien, Silvie Cafarella, and Andrew Tedstone. 2020. "Characterizing Winter Landfast Sea-Ice Surface Roughness in the Canadian Arctic Archipelago Using Sentinel-1 Synthetic Aperture Radar and the Multi-Angle Imaging SpectroRadiometer." *Annals of Glaciology*. https://doi.org/10.1017/aog.2020.48.

Shokr, Mohammed, and Nirmal Sinha. 2015. "Sea Ice Physics and Remote Sensing." *Sea Ice*. https://doi.org/10.1002/9781119028000.ch1.

Similä, M., M. Leppäranta, H. B. Granberg, and J. E. Lewis. 1992. "The Relation between SAR Imagery and Regional Sea Ice Ridging Characteristics from BEPERS-88." *International Journal of Remote Sensing* 13 (13): 2415–32. https://doi.org/10.1080/01431169208904279.

Smith, Benjamin, Helen A. Fricker, Nicholas Holschuh, Alex S. Gardner, Susheel Adusumilli, Kelly M. Brunt, Beata Csatho, et al. 2019. "Land Ice Height-Retrieval Algorithm for NASA's ICESat-2 Photon-Counting Laser Altimeter." *Remote Sensing of Environment* 233 (November 2018): 111352. https://doi.org/10.1016/j.rse.2019.111352.

Stewart, E. J., S. E.L. Howell, D. Draper, J. Yackel, and A. Tivy. 2007. "Sea Ice in Canada's Arctic: Implications for Cruise Tourism." *Arctic* 60 (4): 370–80. https://doi.org/10.14430/arctic194.

Strub-Klein, Lucie, and Denise Sudom. 2012. "A Comprehensive Analysis of the Morphology of First-Year Sea Ice Ridges." *Cold Regions Science and Technology* 82: 94–109. https://doi.org/10.1016/j.coldregions.2012.05.014.

Sudom, Denise, Garry Timco, B Sand, and Lennart Fransson. 2011. "Analysis of First-Year and Old Ice Ridge Characteristics." *Proceedings of the 21th International Conference on Port and Ocean Engineering under Arctic Conditions*.

Sun, Y. 1996. "Automatic Ice Motion Retrieval from Ers-1 Sar Images Using the Optical Flow Method." *International Journal of Remote Sensing* 17 (11): 2059–87. https://doi.org/10.1080/01431169608948759.

Tedesco. 2015. "Remote Sensing and the Cryosphere-Chap.1," no. 2015: 1–16.

Timco, G. W., and W. F. Weeks. 2010. “A Review of the Engineering Properties of Sea Ice.” *Cold Regions Science and Technology* 60 (2): 107–29. https://doi.org/10.1016/j.coldregions.2009.10.003.

Tsamados, Michel, Daniel L. Feltham, David Schroeder, Daniela Flocco, Sinead L. Farrell, Nathan Kurtz, Seymour W. Laxon, and Sheldon Bacon. 2014. “Impact of Variable Atmospheric and Oceanic Form Drag on Simulations of Arctic Sea Ice.” *Journal of Physical Oceanography* 44 (5): 1329–53. https://doi.org/10.1175/JPO-D-13-0215.1.

Ulaby, F. T.;, R. K.; Moore, and A. K. Fung. 1986. “Microwave Remote Sensing: Active and Passive. Volume I: Microwave Remote Sensing Fundamentals and Radiometry.” Edited by Dedham. *Microwave Remote Sensing: Active and Passive. Volume I: Microwave Remote Sensing Fundamentals and Radiometry.*, 470.

Wadhams, Peter, and Josefino C. Comiso. 1992. “The Ice Thickness Distribution Inferred Using Remote Sensing Techniques.” In , 375–83. https://doi.org/10.1029/GM068p0375.

Weeks, W. F., and S. F. Ackley. 1986. “The Growth, Structure, and Properties of Sea Ice.” In *The Geophysics of Sea Ice*, edited by N. Untersteiner, 9–164. New York: Springer. https://doi.org/10.1007/978-1-4899-5352-0_2.

Westoby, M. J., J. Brasington, N. F. Glasser, M. J. Hambrey, and J. M. Reynolds. 2012. “‘Structure-from-Motion’ Photogrammetry: A Low-Cost, Effective Tool for Geoscience Applications.” *Geomorphology* 179 (April): 300–314. https://doi.org/10.1016/j.geomorph.2012.08.021.

Winebrenner, D. P., B. Holt, and E. D. Nelson. 1996. “Observation of Autumn Freeze-up in the Beaufort and Chukchi Seas Using the ERS 1 Synthetic Aperture Radar.” *Journal of Geophysical Research C: Oceans* 101 (C7): 16401–19. https://doi.org/10.1029/96JC01292.

WMO. 1970. “Sea-Ice Nomenclature: Snapshot of the WMO Sea Ice Nomenclature – Terminology and Codes; Volume II – Illustrated Glossary and III – International System of Sea-Ice Symbols)” 1 (259): 121pp.

———. 2010. “Sea-Ice Information Services in the World,” 2010.

https://doi.org/10.25607/OBP-1326.

Yang, Ting-Yi. 2020. “Satellite Altimetry Applications on Lake Ice Thickness and Land Subsidence.” The Ohio State University.

Zakharova, Elena A., Sara Fleury, Kévin Guerreiro, Sascha Willmes, Frédérique Rémy, Alexei V. Kouraev, and Günther Heinemann. 2015. “Sea Ice Leads Detection Using SARAL/AltiKa Altimeter.” *Marine Geodesy* 38: 522–33. https://doi.org/10.1080/01490419.2015.1019655.

Zwally, H. J., B. Schutz, W. Abdalati, J. Abshire, C. Bentley, A. Brenner, J. Bufton, et al. 2002. “ICESat’s Laser Measurements of Polar Ice, Atmosphere, Ocean, and Land.” *Journal of Geodynamics* 34 (3–4): 405–45. https://doi.org/10.1016/S0264-3707(02)00042-X.

Zygmuntowska, M., P. Rampal, N. Ivanova, and L. H. Smedsrud. 2014. “Uncertainties in Arctic Sea Ice Thickness and Volume: New Estimates and Implications for Trends.” *Cryosphere* 8 (2): 705–20. https://doi.org/10.5194/tc-8-705-2014.

Appendix

Copyrighted Material and Author Contribution

I compiled the written document, processed all data types (such as radar imaging and laser altimeter data), helped with study design, carried out study area, research, and analysis, and processed all data types. The research design was overseen by Dr. Randall Scharien, who also provided direction during the analysis and provided meticulous editing during the writing phase. Images of RCM and ASCAT were donated by Akaterini Tavri. Chapter 4 includes content from a future paper submitted co Authoring with Dr. Grant Mcdonald.